MODELING A SPACE-BASED QUANTUM LINK

THESIS

Alexander W. Duchane, Capt, USAF

AFIT-ENG-MS-18-M-020

DEPARTMENT OF THE AIR FORCE
AIR UNIVERSITY

AIR FORCE INSTITUTE OF TECHNOLOGY

Wright-Patterson Air Force Base, Ohio

AFIT-ENG-MS-18-M-020

MODELING A SPACE-BASED QUANTUM LINK

THESIS

Presented to the Faculty

Department of Electrical and Computer Engineering

Graduate School of Engineering and Management

Air Force Institute of Technology

Air University

Air Education and Training Command

in Partial Fulfillment of the Requirements for the

Degree of Master of Science in Electrical Engineering

Alexander W. Duchane, B.S.E.E.

Capt, USAF

March 2018

AFIT-ENG-MS-18-M-020

MODELING A SPACE-BASED QUANTUM LINK

THESIS

Alexander W. Duchane, B.S.E.E.
Capt, USAF

Committee Membership:

Douglas D. Hodson, PhD
Chair

Logan O. Mailloux, PhD
Member

Michael R. Grimaila, PhD, CISM, CISSP
Member

AFIT-ENG-MS-18-M-020

Abstract

Quantum sources and single photon detectors have improved, allowing quantum algorithms for communication, encryption, computing, and sensing to transition from theory and small-scale laboratory experiments to field experiments. One such quantum algorithm, Quantum Key Distribution, uses optical pulses to generate shared random bit strings between two locations. These shared bit strings can be turned into encryption keys to be used as a one-time-pad or integrated with symmetric encryption techniques such as the Advanced Encryption Standard. This method of key generation and encryption is resistant to future advances in quantum computing which significantly degrade the effectiveness of current asymmetric key sharing techniques. This research first reviews previous and current efforts in free-space Quantum Key Distribution. Next, a derivation of the propagation and atmospheric simulation techniques used to model the propagation of an optical pulse from a LEO satellite to ground through turbulence is provided. An Adaptive Optics system, including both lower order tracking as well as higher order corrections using a Self-Referencing Interferometer, is modeled to correct for the aberrations caused by the atmosphere. The propagation, atmospheric, and adaptive optics models are then organized into a general optical propagation toolkit. Satellite positions are calculated using the Simplified General Perturbations model and are used with the optical propagation models to show the effects of using an adaptive optics system during a realistic satellite pass. Finally, the results from the models are compared to experimental data taken from a recent Japanese satellite experiment.

.

Table of Contents

List of Figures

Figure Page

List of Tables

List of Abbreviations

ALF Atomic Line Filter

AFIT Air Force Institute of Technology

AFRL Air Force Research Lab

AO Adaptive Optics

APD Avalanche Photodiode Detectors

DFT Discrete Fourier Transform

DM Deformable Mirror

FT Fourier Transform

FFT Fast Fourier Transform

IJK Geocentric Equatorial Coordinate System

LANL Los Alamos National Labs

LEO Low Earth Orbit

M&S Modeling and Simulation

NICT National Institute of Information and Communications Technology

OTF Optical Transfer Function

RMS Root Mean Squared

PSF Point Spread Function

QBER Quantum Bit Error Rate

QKD Quantum Key Distribution

SEZ Topocentric Horizon

SGP4 Simplified General Perturbations

SKR Secure Key Rate

SLC Submarine Laser Communication

SOR Starfire Optical Range

SRI Self Referencing Interferometer

SNR Signal to Noise Ratio

TLE Two-Line Element set

WFS Wavefron Sensor

SOCRATES Space Optical Communications Research Advanced Technology Satellite

SOTA Small Optical TrAnsponder

SSO Space Surveillance Operations

MODELING A SPACE-BASED QUANTUM LINK

I. Introduction

As optical device technologies such as optical waveguides, single photon detectors, and single photon transmitters matures, applications of systems that use these technologies becomes more prevalent. One of these applied systems, Quantum Key Distribution (QKD), uses the probabilistic nature of light to generate random bit strings between a transmitter, Alice, and a receiver, Bob. Information theory combined with any discrepancies in the bit strings between Alice and Bob can be used to determine the upper bound on the amount of information known by an eavesdropper, Eve. Over the past several years the advancement of single photon transmitters and Avalanche Photodiode Detectors (APD) has led to an explosion of free-space, ground-to-ground, and even space-to-ground experiments [1–16]. A review of these experiments is provided in Ch. II.

The increase in field and space experiments also necessitates the need for Modeling and Simulation (M&S) tools to study QKD and free-space optical systems. Such M&S tools allow for better understanding of the experimental results, provide a means to determine the benefits of advancing technologies still under development, and provides an inexpensive environment to understand the system trade-space in order to determine where novel protocols could enhance secure key generation rates [17–19]. Protocol research can also greatly benefit when modeling the link as a set of discrete events and not long-term or infinite key averages [4, 20]. The protocols in realized QKD systems need to be robust enough to handle variances in the error rate over finite time intervals, and this robustness cannot be determined when looking at infinite length keys.

In this thesis, a Low Earth Orbit (LEO) to ground satellite link scenario is defined,

modeled, and simulated. Specifically, the track of the Iridium 5 satellite over Boulder, CO is used for the experimental link scenario. Boulder, CO is chosen because a model has been developed, using data for the atmosphere in this region, increasing the accuracy of the atmospheric modeling [21]. The Iridium 5 satellite was chosen because its orbit gives many good passes over Boulder, CO, increasing the opportunity for secure key generation. Chs. III and IV describe the process used to determine the best atmospheric and propagation techniques for the model. In Ch. V an Adaptive Optics (AO) system is modeled to measure and correct aberrations caused by the atmosphere. In Ch. VI the Simplified General Perturbations (SGP4) model is used to generate an orbit instance of the Iridium 5 satellite over Boulder, CO. The orbit results are then passed into the models developed in chapters III, IV, and V to estimate quantum throughput along the pass. A comparison of the quantum throughput with and without AO is shown in chapter VII. In Ch. VIII the Iridium 5 satellite over Boulder, CO is swapped for the Space Optical Communications Research Advanced Technology Satellite (SOCRATES) satellite over Tokyo, Japan. The results of a recent Japanese experiment are then compared against the results of the models developed, which show agreement over the center of the pass [22]. Finally, conclusions and further recommendations are offered in Ch. IX.

II. Review of Related Research

The development of loss-tolerant QKD protocols such as the decoy-state protocol and more efficient optical devices has allowed QKD to transition from laboratory to field experiments. This transition has accelerated in recent years, culminating with the seminal Chinese satellite experiments throughout 2016-2017 [14–16]. The first group to perform QKD over a free-space link was Los Alamos National Labs (LANL) in 2002 which was important to understanding the effectiveness of QKD using free-space links [12]. However, there were two issues with this early seminal experiment. The first, as highlighted in "Practical free-space quantum key distribution over 10 km in daylight and at night," the experiment was primarily limited to nighttime operation. While there was some daytime testing performed, it was done in somewhat unrealistic and favorable conditions to minimize background light scattering into the receiver. Even during nighttime, the background light was enough to raise the Quantum Bit Error Rate (QBER) too high and prevent key generation.

The second issue with the experiment is a little more nuanced; it was performed before the decoy state protocol was introduced. In order to get the BB84 protocol to work, LANL did not assume Eve had control over channel losses. Removing this assumption means that multi-photon pulse losses are the same as those seen by a single photon pulse. This assumption is more valid in a free-space experiment where Eve has to place herself in the beam path without being seen as opposed to a fiber implementation where Eve could splice into a fiber and much more easily evade detection. However, with the advent of the decoy state protocol, this assumption no longer needs to be made. In the decoy-state protocol, decoy-state pulses with mean photon numbers different from the signal pulse, are used where the different gains of these decoy pulses can be measured and compared to the gain of the signal pulse [3]. The variance in the gain between the decoy pulses and signal pulse is then used to more accurately bound the presence of an eavesdropper over

the original BB84 protocol, while maximizing the photon throughput [13]. After LANL's first implementation, other groups followed with more robust protocols, specifically the entanglement and decoy state protocols.

In 2005, a 13km free-space entanglement experiment was conducted and in 2007 a 144km decoy state experiment was published [2, 5]. Both experiments no longer had to make assumptions about Eve's control of the channel. However, both experiments still had issues with background light and had to be performed at night with a low Secure Key Rate (SKR); for example, the 144km experiment had a final SKR of 42bits/s [2]. The entanglement experiment was even slower with a SKR of 10bits/s, although with a brighter entanglement source they believed they could achieve a SKR of hundreds of bits/s [5]. Because satellite passes are only a couple hundred seconds long for LEO passes, the SKR needs to be as high as possible for continued secure satellite operations and communications. If multiple passes become necessary, then fewer satellites could be re-keyed over a period of time, reducing the likelihood of re-keying a constellation within a certain period of time. While these two experiments were critical to validating some of the more theoretically robust QKD protocols, they did not consider other essential aspects of a space based system [2, 5].

Other experiments which continued in validating feasibility towards a ground to space QKD demo, including several M&S efforts, have been ongoing in parallel to these lab and field experiments [6, 8, 23] . Two research groups focusing heavily on the daytime QKD dialogue are the Air Force Research Lab (AFRL) and a Chinese consortium [5, 7, 9–11, 13–16].

The AFRL group has two M&S based free-space studies, each of which presents different sets of technologies that can be used to reduce stray background light from reaching detectors [10, 11]. This is important because Alice and Bob cannot tell the difference between signal photons and background noise at their detectors, where noise causes errors

assumed to be from Eve. Because of the necessary security assumptions, the SKR can drop to zero in some cases, even if Eve is not present. The first technology modeled, is an Atomic Line Filter (ALF) [10]. An ALF filters light, to only allow wavelengths of a couple of picometers around the center wavelength to pass through. Because of this, the filter itself, can greatly improve the SKR of a QKD system [10]. However, because the wavelength of a photon is related to its energy, this time-energy uncertainty relationship limits how much temporal filtering can be performed when the spectral filtering is too narrow [10, 11]. Temporal filtering reduces the time Bob looks for a photon and thus filters background noise and improves the overall system rate. If a secure key can be generated, then increasing the system rate linearly increases the SKR. Ultimately, using an ALF for spectral filtering both significantly reduces noise and limits the system's maximum performance.

Another way to filter incoming light that is independent of the time-energy uncertainty relationship is spatial filtering. Spatial filtering can be thought of as looking through a soda straw of ever shrinking diameter [24]. As the diameter decreases so does background noise. However, at a certain point, shrinking the diameter of the soda straw starts reducing the incoming signal. Because the atmosphere causes the signal beam to be spatially broadened, the "soda straw" must be appropriately sized to account for this effect. AO, pioneered at Starfire Optical Range (SOR) [24], is a means of countering the effects of the atmosphere to improve signal throughput while also minimizing background noise [11, 25]. AO allows one to look through a smaller "soda straw" and still reatin a high signal throughput [24]. SOR's papers [10, 11], indicate through M&S, that it is possible for a QKD system to operate robustly in a daytime environment.

While AFRL is using M&S tools to show how a QKD system could be designed to operate robustly, the Chinese consortium has already demonstrated QKD systems operating in daytime conditions [5, 7, 9]. These experiments are important because the channel losses of the experiment approximates those of a LEO engagement. The first experiment also

uses a hot air balloon to approximate the jitter that would be seen in a satellite pass and the second uses an airplane to approximate the slew rates that a telescope would have to keep up with in a LEO pass [7]. Additionally, attention is paid to wavelength choice to reduce Rayleigh scatter and improve the transmission efficiency [9]. Rayleigh scatter is highly wavelength dependent, so choosing longer wavelengths reduces its effect on the quantum channel. Longer wavelengths are also less perturbed by the atmosphere. Unfortunately longer wavelength cameras have lower efficiencies and are noisier than Silicon-based based detectors in the 800nm range, so the choice of 1550nm requires the use of a waveguide to up-convert the 1550nm photon to an 810nm photon which resulted in only 8% capture efficiency [9]. Even with this inefficiency, they were still able to generate secure keys with a SKR of 297bits/s in daylight. As waveguides and photon detector technology improves, so too should their capture efficiency and resulting SKR. For their recent seminal LEO to ground experiment, a wavelength of 850 nm was used for increased detector efficiency [15]. While this research is separate from the research ongoing at AFRL, the two efforts do support each others conclusions that QKD systems can be built to operate robustly in daytime environments.

An additional M&S tool to look at the security of QKD protocols such as the decoy-state protocol has been developed at Air Force Institute of Technology (AFIT) [4, 20]. Specifically the M&S tool looks to determine the validity of infinite key assumptions in lossy channels. A satellite pass has both a finite duration and a very lossy channel. Due to this, if the percentage of decoy-state pulses is too low, then not enough decoy pulses will be measured to accurately measure the gain of the channel [4]. And if the gain of the different states cannot be measured then the protocol loses its security and increased key rate over the standard BB84 protocol. This effect, missing in [10, 11], has necessitated practical implementations of the decoy-state protocol use higher percentages of decoy states then theory dictates [15].

The goal of this thesis is to model entanglement and other novel protocols and compare them to the decoy-state protocol to determine the best protocol for space-to-ground links. Another goal is to determine the percentage of decoy-state pulses that maximizes the SKR without compromising security. In order to do this the propagation and atmospheric models described in [10, 11] need to be integrated with the finite key M&S tool described in [4]. While a fully discretized QKD experiment wasn't able to be carried out in this thesis, the M&S tools developed provide a strong start for a future researcher to complete the integrated model.

III. Atmospheric Model

The first step in simulating beam propagation through the atmosphere is in determining the significant parameters required to model it for the intended purpose. For this study, the engagement scenario is defined as a LEO satellite, Iridium 5, propagating a beam to the ground. This chapter addresses the atmospheric model from space to ground while the generation of orbital parameters for a specific pass is outlined in Chapter VI. The source in the satellite is a 1mm fiber laser with a wavelength, λ, of 780nm. The source is simulated as a Gaussian beam with standard deviation of 0.1mm and propagates 1m from the end of the fiber to a 10cm transmit aperture on the satellite. The beam then propagates to a receive aperture on the ground with a diameter of 1m. A challenging elevation of interest is 60° from zenith, giving a range of 740Km. This elevation is challenging because the farther the satellite is away from zenith, or the closer it is to the horizon, the worse the atmospheric statistics.

Atmospheric parameters are determined using a C_n^2 profile. The C_n^2 is the refractive-index structure parameter and is a measurement of the strength of refractive index fluctuations [26]. The equation for the C_n^2 profile is shown in Eq. (1) where h is the elevation, v is the Root Mean Squared (RMS) windspeed (or pseudowind), and A is free parameter to account for turbulence. For this scenario, v is set to 21m/s and A is set to $1.7 * 10^{-14} m^{-2/3}$ making it the H-$V_{5/7}$ turbulence profile. The H-$V_{5/7}$ turbulence profile is experimentally determined from data collected in Boulder, CO [21]. The H-$V_{5/7}$ name comes from the coherence diameter and isoplanatic angle statistics that result from the choice of A and v. Specifically, the coherence diameter, r_0, equals 5cm and the isoplanatic angle, θ_0, equals 7μrad when looking straight up at a wavelength of 500nm. The coherence diameter is the area over which the light is considered spatially coherent and the isoplanatic angle is the viewing angle over which the light is considered spatially coherent [26]. The coherence diameter is an important parameter to account for the strength of turbulence, with the Rytov

parameter being another. The Rytov parameter, σ_I^2, represents the amplitude fluctuations in light [26]. The atmospheric turbulence is considered weak if $\sigma_I^2 < .25$ and strong if $\sigma_I^2 \gg .25$ [27]. The amplitude fluctuations are considered fully developed if $\sigma_I^2 = 1$. The equations for r_0 and σ_I^2 are shown in Eqs. (2,3) [26].

$$C_n^2(h) = 0.00594(v/27)^2 * (10^{-5}h)^{10} * e^{-h/1000} + 2.7 * 10^{-16} * e^{-h/1500} + A * e^{-h/100} \quad (1)$$

$$r_{0,pw} = \left[sec(\zeta) * .423 * k^2 * \int_0^H C_n^2(h)dh\right]^{-3/5} \quad (2)$$

$$\sigma_I^2 = 2.25 * k^{7/6} * sec^{11/6}(\zeta) \int_0^H C_n^2(h) * h^{5/6}dh \quad (3)$$

In Eq. (2), ζ refers to the angle off of zenith and in Eqs. (2, 3) H refers to the final propagation elevation and is equal to $z * cos(\zeta)$ where z is the propagation distance. For a wavelength of 780nm and $\zeta = 60$ degrees, $r_{0,pw} = 5.58$cm and $\sigma_I^2 = .493$. These two atmospheric parameters are used to solve a system of equations and generate a set of intermediate phase screens, giving the final $r_{0,pw}$ and σ_I^2 [27]. Because the atmosphere thins and minimally effects the beam above 20Km, phase screens modeling only the last 20Km of the propagation are generated. Even though the propagation distance through the atmosphere is greater than 20km for $\zeta > 0$, the calculations for the coherence diameter and scintillation will account for increased atmospheric effects and modify the $r_{0,i}$ values to give the proper atmospheric effects. For this example, the $r_{0,i}$ values are 5.95cm, 24.40cm, and 69.86cm.

With the atmospheric and engagement parameters set and the propagation models determined, phase screens modeled statistically using the Kolmogorov Fourier technique are generated [26, 27]. A grid of Gaussian random numbers with zero mean and unit variance is generated and multiplied by the Von Karman spatial frequency of each grid point. The equation for the Von Karman spectrum is shown in Eq. (4), where Φ_n is the refractive-index spectrum, f is the spatial frequency of the grid point in cycles/m, f_m is the inner

scale frequency and f_0 is the outer scale frequency parameter [27]. The inner scale and outer scale parameters are the frequencies of the smallest and largest turbulent eddies in the atmosphere. If f_0 and f_m are estimated at ∞ and 0 respectively, then the Von Karmon spectrum simplifies to the Kolmogorov spectrum [26]. Because the grid used in the simulations has a large number of points, the Kolmogorov phase screens capture high frequency components well. But at the center of the grid, the denominator in Eq. (4) goes to zero, causing the $\Phi_n \to \infty$. If the inverse Fourier transform is taken with the singularity in the grid, the resulting phase screen is of no value. If the center point is manually set to zero, then the phase screen is useable; however, low frequency information is lost when manually setting the center value. Some of the information can be gained back by looping through sub-harmonics of the larger phase screen and adding them to the high-frequency screens [27].

$$\Phi_n = 0.23 * r_0^{-5/3} \frac{e^{-(f/f_m)^2}}{(f^2 + f_0^2)^{11/6}} \tag{4}$$

An additional atmospheric parameter of interest is the Greenwood frequency, f_G. Similar to the coherence diameter, the Greenwood frequency describes the coherence time of the atmosphere. After a time interval equal to or greater than f_G the atmosphere is no longer statistically related to a previous draw of the atmosphere, and a new phase screen needs to be generated. The equation for f_G is shown in Eq. (5), where $V_\perp$ is the transverse wind velocity [26]. Because the satellite's transverse velocity with respect to the ground site changes over the pass, so does the effective $V_\perp$ and f_G. And because the satellite's transverse velocity increases near zenith, f_G becomes more challenging at zenith. This is different from $r_{0,pw}$ and σ_I^2 which become more benign closer to zenith. The equation for $V_\perp$ is shown in Eq. (6) [26]. $V(h)$ in Eq. (6), can be described by the Bufton wind model as shown in Eq. (7) [26, 28]. The Bufton wind model is based off of balloon experiments

conducted in southeastern New Mexico [28]. Because New Mexico and Colorado have similar atmospheres, the use of the Bufton wind model fits well with the use of the H-$V_{5/7}$ turbulence profile. In Eq. (7) ω_s is the slew rate of the satellite and V_g is the ground wind speed where $V_g = 5m/s$ for the H-$V_{5/7}$ turbulence profile. The calculation of the slew rate is described further in chapter VI. The Greenwood frequency is approximately 36Hz for $\zeta = 60$ degrees; however it can be over 750Hz near zenith.

$$f_G = \frac{V_\perp}{0.32 r_0} \tag{5}$$

$$V_\perp = \left[\frac{1}{15 * 10^3} \int_{5*10^3}^{20*10^3} V^2(h) dh \right]^{1/2} \tag{6}$$

$$V(h) = \omega_s h + V_g + 30 e^{-(\frac{h-9400}{4800})^2} \tag{7}$$

IV. Propagation Model

With the engagement and atmospheric scenario parameters set, the optimal propagation techniques for each part of the beam path are determined. The first part of the beam path is from the fiber to the satellite transmit aperture. Since the propagation is relatively short compared to the spatial frequencies of the source, both the Fresnel and angular spectrum propagation techniques work well. The Fresnel technique multiplies the source field by a quadratic phase term then performs a Fast Fourier Transform (FFT) to determine the target field [27, 29]. However, because it performs just a single FFT the target plane spacings are set by the source plane. Using the angular spectrum method, the field is multiplied by a quadratic phase factor, Fourier transformed, multiplied by a second quadratic phase factor, and then inverse Fourier transformed [27, 29]. Essentially, the beam is deconstructed into an infinite number of plane waves, each is propagated, and then the waves are added together to construct the propagated field. With the addition of a scaling parameter, the target spacing is no longer strictly set by the source spacing, but is bounded by four inequalities [27]. Equations (8-11) show the bounding requirements for the source spacing, δ_1, target spacing, δ_2, given the source and target diameters of interest, D_1 and D_2, the focal length, R, and the number of grid points, N. Fig. 1 illustrates the inequalities from Eqs. (8-11). With an initial spacing of 1μm, a final spacing of 625μm, and at least 1024 grid points, all requirements are satisfied. The purpose of the Gaussian intensity profile initially given to the beam is to cause divergence in the propagation between the fiber and transmit aperture. This causes the beam to more evenly fill the transmit aperture, and more efficiently propagate to the ground. However, to accurately model this effect, the transmit grid spacing needs to sample the Gaussian profile. The sample spacing requirement is the standard deviation of the Gaussian beam [30]. For this experiment, the initial transmit beam is modeled as having a standard deviation of 10μm. The original choice of $\delta_1 = 1\mu m$ surpasses the sampling requirement to accurately sample the Gaussian beam.

$$\delta_2 \leq \frac{-D_2}{2D_1}\delta_1 + \frac{\lambda \Delta z}{D_1} \tag{8}$$

$$N \geq \frac{D_1}{2\delta_1} + \frac{D_2}{2\delta_2} + \frac{\lambda \Delta z}{2\delta_1 \delta_2} \tag{9}$$

$$\left(1 + \frac{\Delta z}{R}\right)\delta_1 - \frac{\lambda \Delta z}{D_1} \leq \delta_2 \leq \left(1 + \frac{\Delta z}{R}\right)\delta_1 + \frac{\lambda \Delta z}{D_1} \leq \delta_2 \tag{10}$$

$$N \geq \frac{\lambda \Delta z}{\delta_1 \delta_2} \tag{11}$$

Modeling the second propagation from the transmit aperture to the top of the atmosphere is more challenging. The high frequency components due to the small source diameter cause aliasing effects after the long propagation. Since both the Fresnel and angular spectrum methods rely on FFTs, both are susceptible to high frequency components wrapping from one side of the grid to the other, causing errors in the target plane field. One way to prevent this is to add extra grid points around the source field to prevent the aliased signal from reaching the area of interest in the center of the grid. Fig. 2 shows the sampling requirements for the propagation from the satellite to the top of the atmosphere if the area of interest at the top of the atmosphere is 2m. The area of interest is chosen to be 2m even though the final area of interest is 1m in order to account for turbulence that might focus energy back into the telescope that would normally diverge away during the final propagation step. In order to make this propagation work, over 11,000 grid points are needed. While feasible, this is not a practical solution, and a different modeling technique is needed.

The path chosen to reduce the number of points necessary to simulate the propagation is to use the Rayleigh-Summerfeld propagation technique. This technique does not use Fourier transforms and is valid when the transmit and receive diameters, as well as, the propagation length are on the order of λ or greater [29]. The other requirement is that the source plane is well sampled to capture the phase and intensity profile. Specifically,

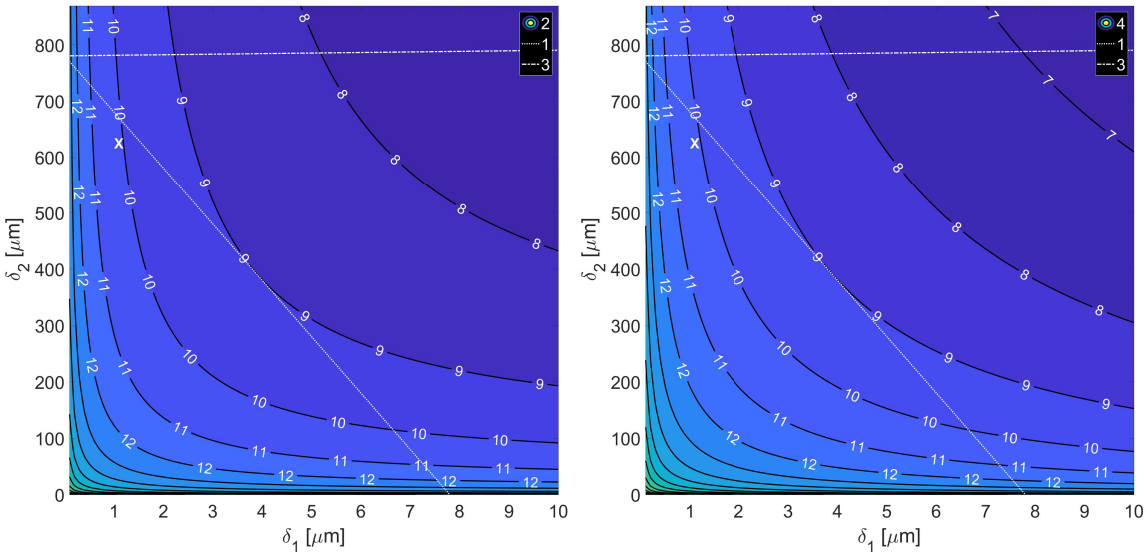

Figure 1. Sampling requirements for propagation from fiber to transmit aperture. Chosen parameters are $\delta_1 = 1 * 10^{-6}$, $\delta_2 = 625 * 10^{-6}$, and $N > 2^{10}$.

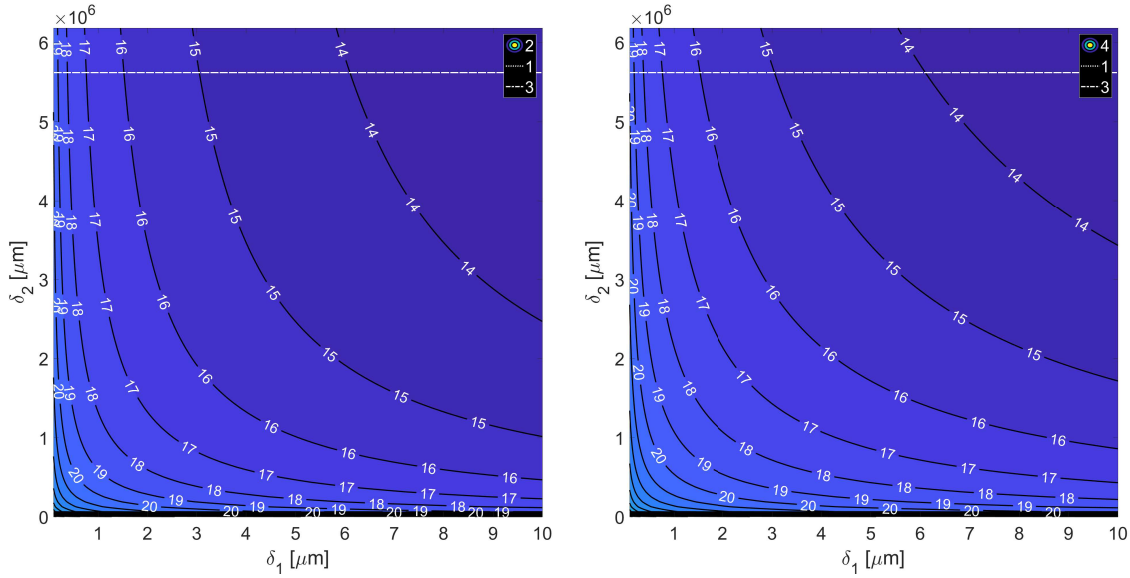

Figure 2. Sampling requirements for propagation from fiber to transmit aperture using angular spectrum method. Constraints 1 and 3 are overlapping.

no phase shifts of greater than π should occur, and any high frequency intensity changes should have multiple points sampling it. Fig. 3 shows the intensity and phase profile of the transmit plane. Where there is intensity, there are no phase shifts of greater than π, and the intensity profile itself is well sampled. The output plane intensity and phase profile are computed using the Rayleigh-Summerfeld technique and shown in Fig. 4. Even though the intensity profile looks like it has some curvature, when looking at the y-axis scaling, it can be seen that the intensity profile is essentially flat across the region of interest. The phase in Fig. 4 is also well sampled, with no phase shifts greater than π.

Fig. 5 shows the sampling requirements for the propagation from the top of the atmosphere to the telescope. The inequalities to be satisfied shown in Fig. 5 are the same as in Fig. 1 with two exceptions. The first is that $D_1 \rightarrow D_1'$ and $D_2 \rightarrow D_2'$ as shown in Eqs. (12) and (13) where c is an adjustable parameter to catch more of the light and $r_{0,rev}$ is the coherence diameter when propagating in the reverse direction [27]. Since the r_0 value is calculated for a plane wave, its value is the same in either direction. This change in inequality accounts for the broadening effects of turbulence. The second change in inequality is the addition of a maximum propagation distance. This equation is shown in Eq. (14) where ΔZ_i is the max propagation distance per step and δ_n is the final plane grid spacing. Given this maximum propagation distance, a minimum necessary number of propagations can be found. The solution for this set of inequalities is a source plane spacing of 1mm, a target plane spacing of 1.5625mm, at least 2372 grid points in each plane, and at least three propagations. Since three phase screens were used to simulate the atmosphere, the necessary number of propagations and number of phase screens match perfectly.

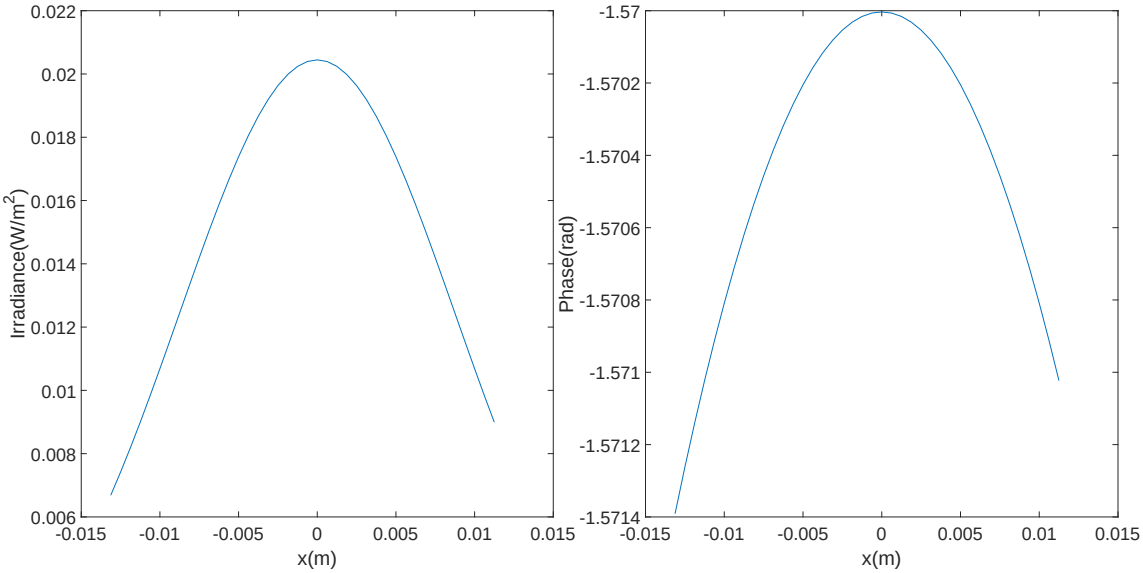

Figure 3. Intensity and phase profile at front of transmit aperture.

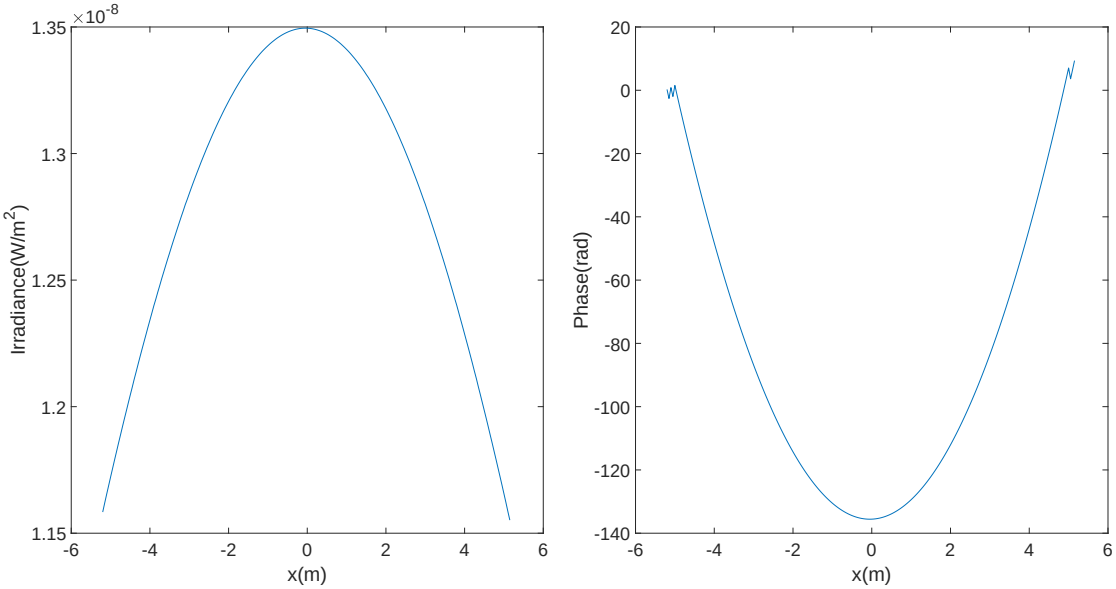

Figure 4. Intensity and phase profile at top of atmosphere.

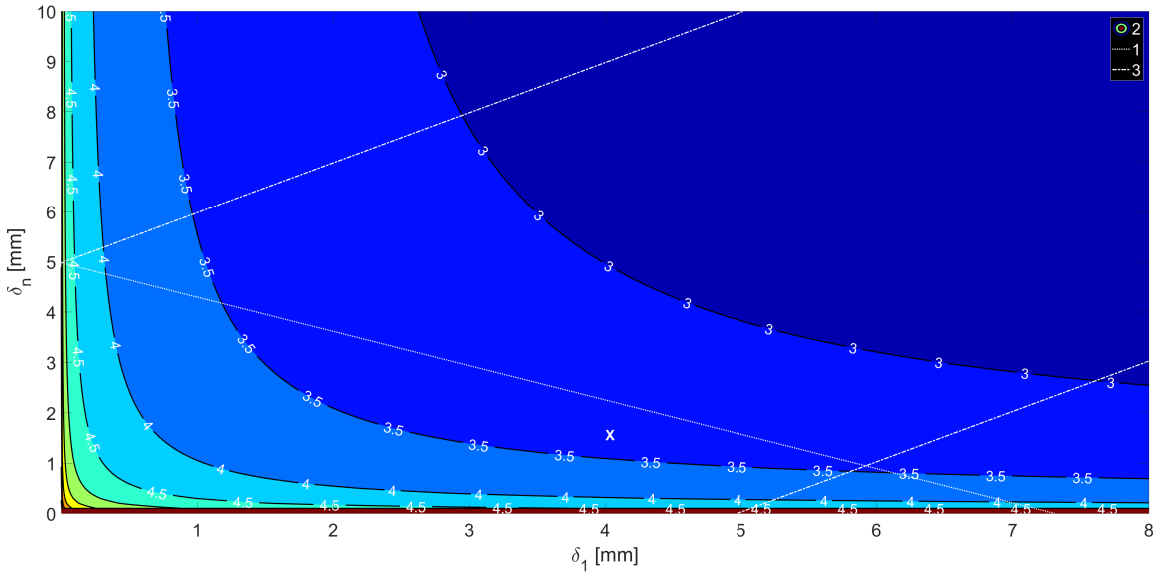

Figure 5. Sampling requirements for propagation from top of the atmosphere to the receiving telescope. Chosen parameters are $\delta_1 = 1 * 10^{-3}$, $\delta_n = 1.5625 * 10^{-3}$, $N > 10^{3.375}$, and at least 3 propagations.

$$D_1' = D_1 + c\frac{\lambda \Delta z}{r_{0,rev}} \tag{12}$$

$$D_2' = D_2 + c\frac{\lambda \Delta z}{r_0} \tag{13}$$

$$\Delta Z_i = \frac{min(\delta_1, \delta_n)^2 * N}{\lambda} \tag{14}$$

The resulting field from the Rayleigh-Summerfeld propagation can be interpolated to the number of grid points required for the third propagation, decreasing the computation time of the propagation. A Discrete Fourier Transform (DFT) interpolation method is used in this model. In a DFT interpolation the field is Fourier transformed, zero padded, then inverse Fourier transformed [30, 31]. This method was chosen since the DFT interpolation method uses the same functions also necessary for the Fourier propagation tools.

The final propagation in the simulation is from the telescope entrance to the focal plane.

The focal plane is used for both tracking as well as the location of the QKD system. Since the number of grid points and initial grid spacing has already been defined by the previous propagation step, and a change would require a recalculation of all previous propagation requirements the angular spectrum method's flexibility is not necessary. Fresnel propagation works with less computation complexity than the angular spectrum method. Eq. (15) shows the equation for a Fresnel propagation where x and y define the output plane and ζ and η define the input plane, and k is the wave-number and is equal to $\frac{2\pi}{\lambda}$. Eq. (15) can be further modified by recognizing that this is the final propagation of a two lens system, where the first lens is the transmit aperture on the satellite and the second is the receiver telescope on the ground [29]. If both telescopes have their focal lengths satisfy the lens makers equation, Eq. (16), then the quadratic phase term in the Fresnel propagation, Eq. (15), is cancelled out by the focus term applied by the receiver telescope. This focus term is found in Eq. (16) by solving for f with $z_1 = 740$km and $z_2 = 5$m. Since $Z_1 \gg Z_2$ then the focal length of the receive telescope should be approximately equal to 5m in order to cancel out the quadratic phase term in Eq. (15). However, this setup does not cancel out any phase aberrations caused by the atmosphere. An AO system is needed.

$$U(x,y) = \frac{e^{\frac{j2\pi z}{\lambda}}}{j\lambda z} \int_{-\infty}^{\infty}\int_{-\infty}^{\infty} U(\zeta,\eta) e^{\frac{jk}{2z}(\zeta^2+\eta^2)} e^{\frac{-jk}{z}(x\zeta+y\eta)} d\zeta d\eta \tag{15}$$

$$\frac{1}{f} = \frac{1}{z_1} + \frac{1}{z_2} \tag{16}$$

Two statistical metrics are used to determine the validity of the simulation. The coherence factor of the beam after propagating through the atmosphere is used in order to determine if the generated phase screens and simulated beam propagation through them accurately describes the expected distortion of the beam due to atmospheric turbulence. A Point Spread Function (PSF) is used to determine the end-to-end accuracy of the simulation

where the simulated PSF of a vacuum and turbulent propagations without AO are compared to the analytic expectations. The PSF results are shown in chapter V where the effects of an AO system on the PSF are compared to the PSF with no correction.

The coherence factor of a beam is a function of the mutual coherence function and describes how strongly one part of the beam is correlated with another [26,27]. This metric is important because it relates to Wavefron Sensor (WFS) camera pixel size and Deformable Mirror (DM) actuator size. If the simulated coherence factor is larger than the analytic coherence factor, then better AO results can be shown with larger DM actuator spacing. The equation for the coherence factor, μ, is shown in Eq. (17), where D is the structure function as described by Eq. (18). In Eq. (18), Δr is the distance from the center of the aperture. Because this is a statistical quantity, multiple atmospheric realizations are necessary for the simulated results to be compared to the analytic ones. Fig. 6 shows a comparison of the analytic and simulated coherence function with 100 atmospheric simulations. The two agree pretty closely when $\Delta r/r_0$ is smaller, but diverge some as $\Delta r/r_0$ increases. This means that the atmospheric simulation more accurately models lower spatial frequencies such as tip and tilt but less accurately models higher frequency turbulence. Some methods to more accurately model the turbulence are to increase the propagation distance through the turbulence, increase the number of phase screens and partial propagations, or shrink the grid spacing [27]. However, these methods increase the complexity and time necessary to run the simulation.

$$\mu = e^{-D/2} \tag{17}$$

$$D = 6.88 * (\Delta r/r_0)^{5/3} \tag{18}$$

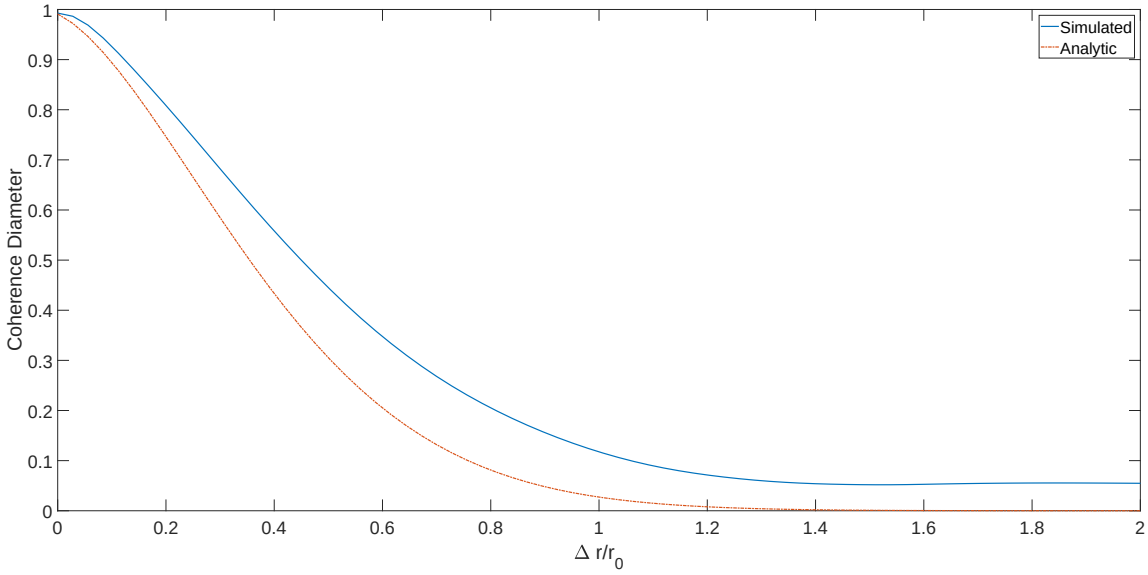

Figure 6. Comparison of analytic and simulated coherence diameter with 100 atmospheric realizations.

V. Tracker and Wavefront Sensor Model

Atmospheric compensation can be broken down further into lower and higer order aboration correction. The tracking system corrects for the lower order atmospheric aberrations of tip and tilt, and the wavefront system corrects for all higher order atmospheric aberrations, limited only by the number of pixels in the wavefront sensor camera and actuators in the DM [25, 32]. In this experimental scenario the tracking camera is in a focal plane while the WFS is in a pupil plane. To simplify the simulation, both systems apply corrections in the pupil plane. The image from the tracking camera measures the centroid of the spot by using Eq. (19) and then determines the gradient in the pupil plan by Eq. (20) [33, 34]. In Eqs. (19 and 20) $\bar{x}$ is the calculated x-shift and in Eq. (20) W_x is the calculated x-gradient in the pupil plane. The y-shift and y-gradient are calculated in an identical manner. In Eq. (19) (I, x, y) is the intensity at each grid point. The intensity in photons can be calculated from the field at the camera by Eq. (21), where $I(x, y)$ is the intensity at each point, $U(x, y)$ is the field, δ_t is the integration time of the tracker, h is Plank's constant, and c is the speed of light. To add noise to the camera, the intensity at the camera is modeled as having a Poissonian distribution. The intensity is multiplied by the Signal to Noise Ratio (SNR) squared, then used as the mean value to generate a Poisson distribution. Random draws of the distribution are made to determine the intensity for each camera pixel [30]. The SNR is left as a free parameter to allow for experimentation. As either the intensity or SNR is decreased, the increased noise will cause errors to the gradient calculation. With the tracker simulated, the next step is to simulate a WFS.

$$\overline{x} = \frac{\sum\sum I(x,y) \cdot x}{\sum\sum I(x,y)} \tag{19}$$

$$W_x = \frac{\overline{x}}{f} \tag{20}$$

$$I(x,y) = \delta_t \frac{|U(x,y)|^2}{hc\lambda} \tag{21}$$

In this simulation a Self Referencing Interferometer (SRI) WFS is modeled [35]. In an SRI WFS incoming light is broken up into two legs. In the first path it is converted into a flat field to be used as a reference beam. In the second leg the signal beam is distributed to four cameras but otherwise unaltered. At each camera the signal beam is interfered with a phase shifted version of the reference beam. With phase shifts of 0, $\frac{\pi}{2}$, π, and $\frac{3\pi}{2}$, a different irradiance pattern is created at each camera. The four-quadrant inverse tangent can then be used to pull the phase information from the four irradiance patterns [35]. Like the tracker, the irradiance can be converted into an intensity pattern, and Poisson noise can be added. In this case, there are four cameras where noise is added which can create large errors in low SNR environments; however, there are environments where the SRI WFS performs much better than the Shack-Hartman WFSsuch as scintillated environments where the SRI is less effected by null intensity points [36]. One important specification for a WFS is the size of the camera pixels and actuators across the pupil plane. If they are larger than r_0, then the atmosphere cannot adequately be sampled and corrected. As the size of the actuators and pixels decreases, the more close the spot can be corrected to diffraction limited. However, as the pixel size is decreased, the irradiance on each pixel is decreased and the SNR goes down. There is also a manufacturing limit to the size of the pixels and actuators that can be created. For this study, the number of actuators and pixels in the SRI is set to 64. With a telescope diameter of 1m this means the pixel and actuator size is effectively 1.56cm, smaller than the 5.58cm r_0. However, the measurements and

corrections occur in a conjugate pupil plane where lenses are used to shrink the beam, so the actual pixels and actuators are on the order of μm [29]. With the atmosphere, propagations, and simulations modeled, the final step is to test the model against analytic expectations.

The PSF of the propagated beam in the focal plane is used to test if the AO system is correcting the atmospheric distortions as well as further test the validity of the atmospheric and propagations models. The PSF is a measure of the spot size at the camera and an analytical solution are calculated by taking the Fourier Transform (FT) of the Optical Transfer Function (OTF). Because the PSF and OTF are FTs of each other, effects that require convolution to calculate the combined PSF, such as aperture and atmospheric effects, can be calculated by multiplying their OTFs [26, 30]. Fig. 7 shows the comparison of the diffraction limited PSF, the analytically calculated PSF, and the PSF calculated. The diffraction limited PSF is calculated by propagating a plane wave through the telescope system where the analytic OTF is found by taking the FT of the diffraction limited PSF then multiplying it by the long-term atmospheric OTF, using Eq. (22) [25, 26, 30]. In Eq. (22), $f_{x,y}$ is the spatial frequency at each grid point and f_l is the focal length. The resulting PSF is then calculated by taking the FT of the analytic OTF. Fig. 7 shows the comparison of the three different PSF calculations. The vacuum PSF is much narrower than the analytically calculated PSF including atmospheric effects, showing just how much the turbulence broadens the spot at the camera. The simulated PSF without AO closely resembles the analytic PSF, but is a little wider and lower. This is likely due the high Rytov value scintillating the beam. With a heavily scintillated beam, more simulations are necessary for the simulated PSF to converge to the analytic PSF. Also, as with Fig. 6, more atmospheric phase screens may be necessary for the statistics to best match the analytic counterparts. Fig. 8 shows a comparison of the vacuum, simulated PSF without AO, and simulated PSF including AO. The AO system does a very good job reducing the spot size, but cannot perfectly reconstruct the beam. This is because the AO system does not have infinite spatial and temporal

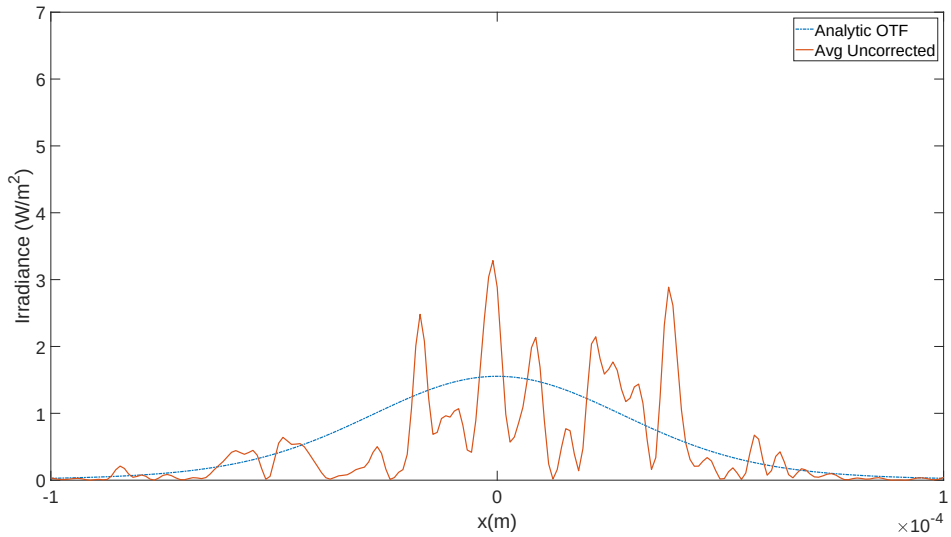

Figure 7. Comparison of analytic and simulated PSF.

bandwidth. The AO system does not have an infinite number of iterations to close the control loop, and has an actuator size smaller than r_0, but much larger than the grid size used to create the phase screens. While multiple experiments can be performed by changing the SNR, the camera pixel and actuator size, and adding in additional sources of loss and noise into the tracking and AO systems, the results of Fig. 8 show that the tracking and AO system are functioning well and can be used to simulate the effects in a real system.

$$H_{LE} = e^{-3.44\left(\frac{\lambda f_l f_{x,y}}{r_0}\right)^{5/3}} \tag{22}$$

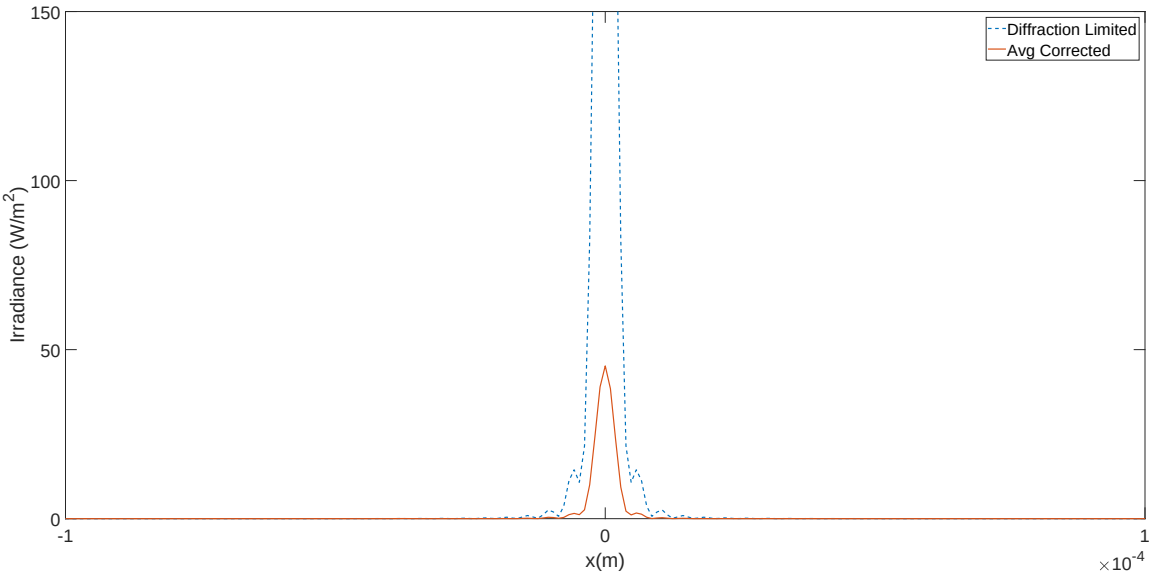

Figure 8. Comparison of diffraction limited, uncompensated, and compensated PSFs.

VI. Satellite Model

With the propagation, atmospheric, and AO modeled the next step is to model a satellite pass (i.e. azimuth, elevation, and range as a function of time) over a ground station. There are three parts to model a satellite pass over a ground station; the modeling of the position and velocity vectors of the satellite over time; modeling the position vector of a ground station over the same time interval; and then overlaying the two in order to get the azimuth, elevation, and range of the satellite from the ground station. The SGP4 model, developed based on Ref. 37, is used.

The purpose of this thesis was not to perform an extensive study of all possible satellite ground tracks over a ground station, but to use existing orbits to simulate satellite passes. The Iridium 5 satellite was chosen because the Iridium mission of providing global communications means that the orbital parameters of the satellites are set to provide maximal ground coverage for a given ground site [38]. Any of the Iridium constellations could have been chosen since they follow a similar ground track, with one following behind the other. With a satellite chosen, the satellite parameters, referred to as a Two-Line Element set (TLE) set, were then used as input into the SGP4 model. The TLE for the Iridium 5 satellite can be downloaded from `www.space-track.org` or `https://www.celestrak.com/NORAD/elements/`. TLE parameters are updated daily as intentional movement and general perturbations from the propagator within the SGP4 model can invalidate old TLEs. The other input for the SGP4 model is the time since epoch or the beginning of the Christian era [37]. The output from the SGP4 code is a position and velocity vector in the Geocentric Equatorial Coordinate System (IJK). However, what is needed for the purpose of this research is the position and velocity of the satellite relative to a ground station.

In order to determine the position and velocity of the Iridium 5 satellite relative to a ground site located in Boulder, CO the satellite and ground station need to be translated

into the Topocentric Horizon (SEZ) coordinate system [37]. This is performed in additional SGP4 models. Like a satellite, the earth deviates from idealistic models over time. Several parameters from `https://www.iers.org/IERS/EN/DataProducts/EarthOrientationData/eop.html` are used to account for the deviations. Specifically the excess length of day and polar motion coefficients are used. The excess length of day is the difference between the astronomical length of day and 24 hours. The polar motion coefficients account for the change in the earth's axis when measured as the normal from the true equator versus the mean surface geographical axis [37]. With these inputs the azimuth and elevation as well as the delta azimuth and delta elevation of the Iridium 5 satellite with respect to Boulder, CO can be found. Fig. 9 shows several satellite passes after running the model at 5 second intervals over one week.

While there are several passes where the satellite rises above 60°, one pass, on day 5, rises above 80°. That specific pass is used as the test pass for the remaining simulations. By coming so close to zenith the pass has the widest variance of atmospheric characteristics. In Fig. 9 it is seen that the magnitude of the change in azimuth and elevation angles spike as the satellite approaches zenith. The square root of the sum of the two rates squared can be used to find the tangential angular velocity of the satellite relative to the ground station. Shown in Eq. 23, ω_s is the same as in Eq. 7 from Chapter III. With this final detail the $r_{0,pw}$, σ_I^2, and f_G values can be determined over the satellite pass.

$$\omega_s = \sqrt{\Delta_{Azimuth}^2 + \Delta_{Elevation}^2} \tag{23}$$

Fig. 10 shows the coherence diameter of the beam over the satellite pass while Figs. 11 and 12 show the scintillation index and Greenwood frequency respectively. The coherence diameter increases and the scintillation index decreases as the satellite approaches zenith. This means that the phase abortions and intensity fluctuations are weaker at zenith then at lower elevation angles. However, the Greenwood frequency spikes toward zenith. While

the atmospheric distortions are weaker, the atmosphere changes much more rapidly. This is expected since the plots follow Eqs. 2 and 3 where $r_{0,pw}$ and σ_I^2 weaken as a function of ζ, the angle from zenith. However, f_G, as described by Eq. 5 is a function of ω_s which spikes near zenith. These competing parameters are important for Chapter VII where AO systems with different capabilities are compared against each other. Not only do the results support the validity of the model, but also provide insight on the performance tradespace of AO systems and their impact on the overall quantum throughput of the system.

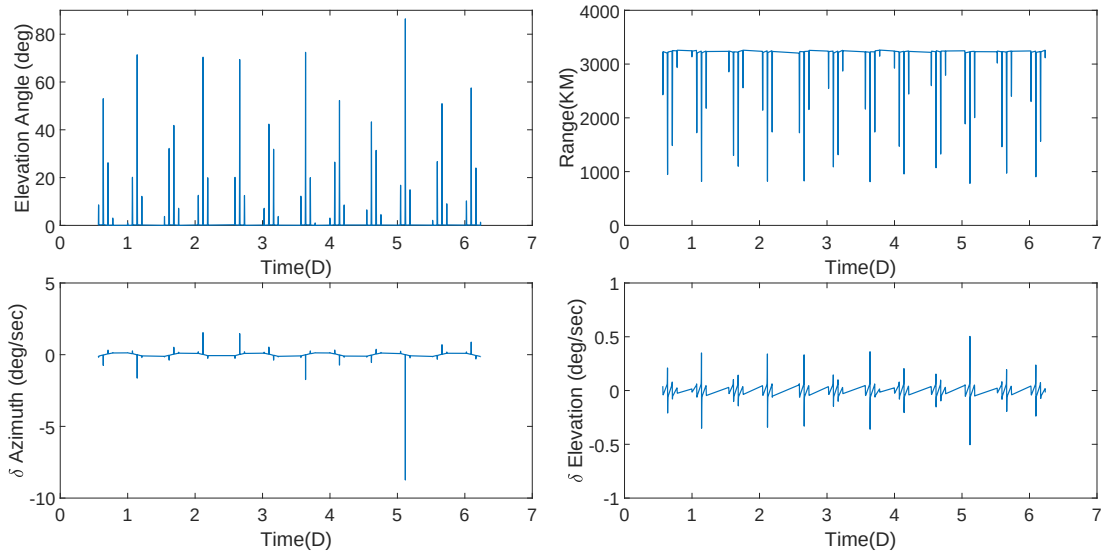

Figure 9. Example of Iriduim 5 Satellite passes over Boulder, CO for one week. Satellite sampled at 5s intervals.

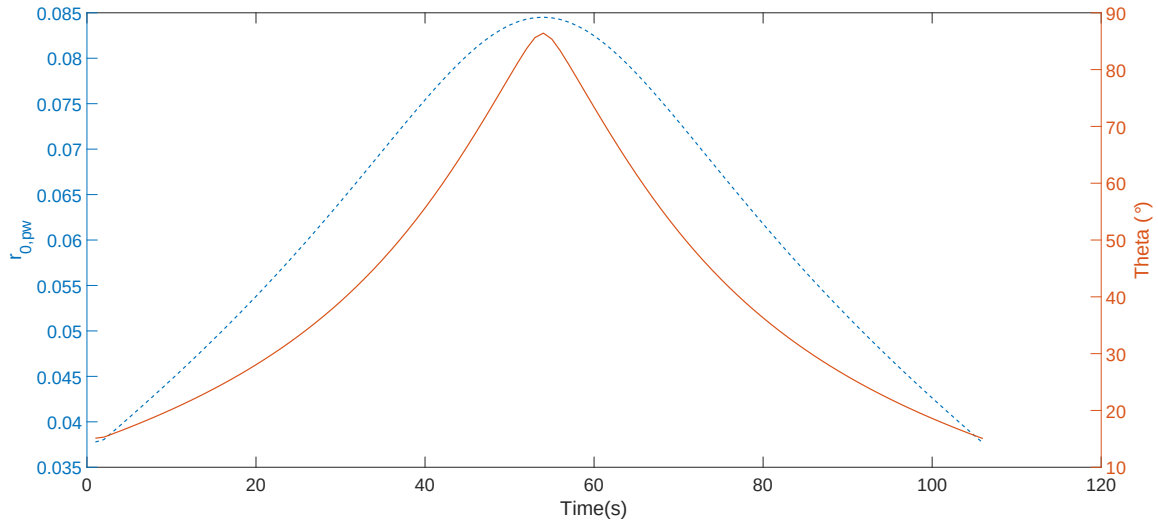

Figure 10. Coherence diameter as a function of time over the satellite pass as compared to elevation angle.

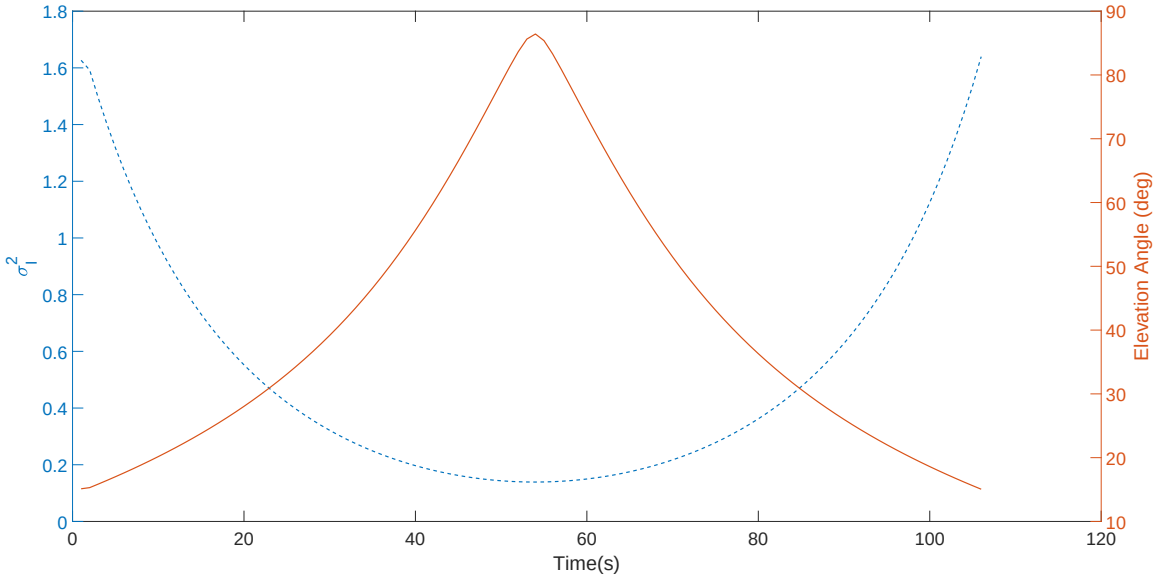

Figure 11. Scintillation index as a function of time over the satellite pass as compared to elevation angle.

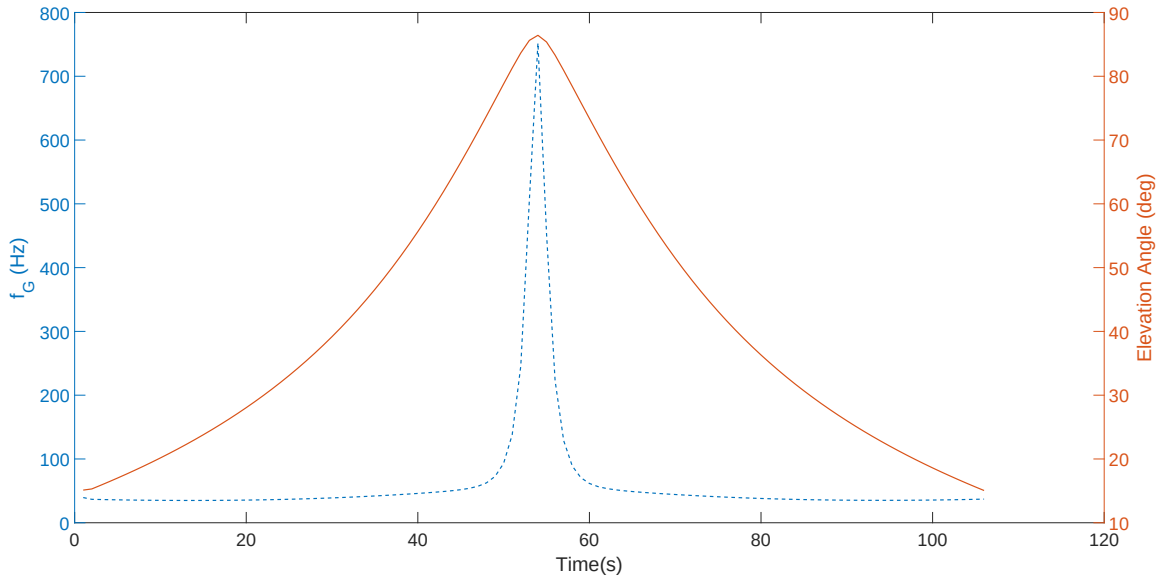

Figure 12. Greenwood frequency as a function of time over the satellite pass as compared to elevation angle.

VII. Simulation Results

With all of the necessary models completed, the next step in the simulation is to use them together to simulate the quantum throughput over a satellite pass. However, two additions from chapter IV need to be considered to ensure they don't invalidate the models. These additions allow for a greater portion of the satellite pass to be studied. The first is that the optical link is modeled for the satellite pass while it is at least 15° above the horizon. The 15° difference between the satellite simulation and initial value of ζ causes $r_{0,pw}$ to be smaller than initially simulated. The smaller value of $r_{0,pw}$ increases the turbulent effects of the atmosphere and requires more grid points as described by Eqs. 8-11 and 12-14. However, the number of grid points used is reduced from 2600 to 2400 to increase the speed of the simulation. In chapters IV and V the coherence factor and PSF are used as quantitative methods to validate the model. Here, a qualitative method is used to determine the validity of the model. Fig. 13 shows the intensity and phase of the field after propagation through the atmosphere with $\zeta = 60^\circ$ and $N = 2600$. In this case all constraints are satisfied. The intensity is speckled and the phase is folded due to the effects of the atmosphere. However, no grating or other artifacts of aliasing are seen. The phase distortions in the corners are caused by the lack of intensity in those regions. Since the phase of a field is determined by the angle between the real and imaginary components, a phase value can be calculated even as the intensity goes to zero. This value loses meaning when there is no intensity; however it causes aliasing in the phase to be noticed before aliasing in the intensity is seen.

Fig. 14 shows the intensity and phase of a field propagated with $\zeta = 75^\circ$ and $N = 2400$. In Fig. 14 the intensity is more speckled and the phase has noticeably tighter ripples than in Fig. 13. This makes sense since the atmosphere is more turbulent in the second figure, so the field should also be more disturbed. However, no aliasing effects are seen, even at the edges of Fig. 14. Thus, one is left to ponder, what would these aliasing effects look like? Could they ever be seen? Fig. 15 shows the intensity and phase of a field propagated with

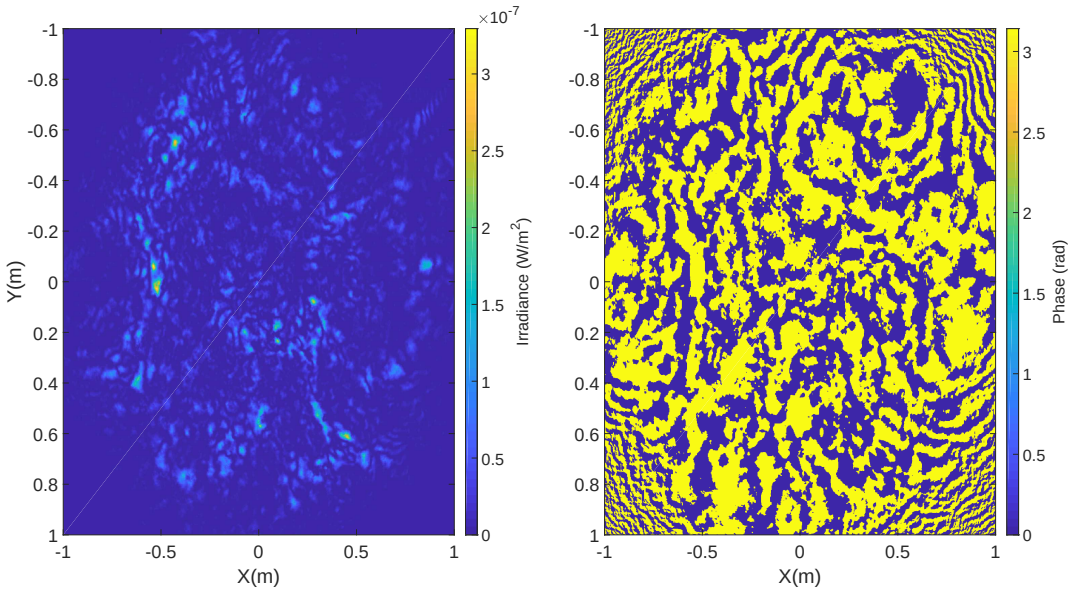

Figure 13. Irradiance (left) and phase (right) of field at front of telescope with all propagation constraints met.

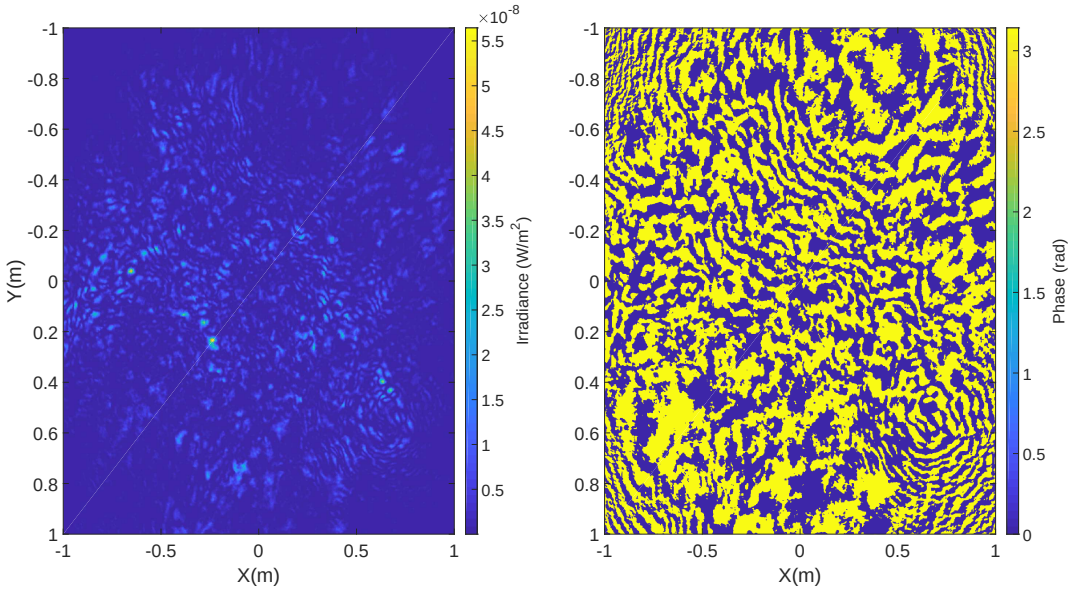

Figure 14. Irradiance (left) and phase (right) of field at front of telescope for $N = 2400$ and $\zeta = 75°$. No aliasing effects are seen in either image.

$\zeta = 75^\circ$ and $n = 1024$. In this case N is now much smaller than the value necessary to satisfy the inequalities in Eqs. 8-11 and 12-14. This causes significant grating effects as seen in Fig. 15. The effects travel all the way to the center of the field, rendering them completely invalid. However, since aliasing effects are not seen at all in Fig. 14, the simulated fields are valid.

Fig. 16 shows the ratio of the throughput with/without AO compared to f_G. There are 100 data points taken at each of 106 satellite positions. The number of unique atmospheres simulated at each satellite position changes as a function of f_G. The SRI is set to 1 KHz update rate with 32 actuators. At lower elevation angles, where f_G is smaller, the SRI can be seen converging to a quantum throughput value for each instance of the atmosphere. But as the satellite approaches zenith and f_G spikes, the SRI control loop is not able to update fast enough to converge before the atmosphere shifts. Other than the convergence of the SRI WFS it is hard to find much more understanding from the figure. The large variations in the quantum throughput make it hard to understand where the AO system is working best and where it is starting to fail. Even when the average of the 100 data points is taken, as shown in Fig. 17, the variations in the quantum would make it hard to compare AO systems with different parameters. One conclusion that can be drawn is that as a satellite's elevation angle increases, the advantage of having an AO system decreases. This makes sense for two reasons. The first is that as the elevation angle increases, so does the $r_{0.pw}$ value. This means there are fewer distortions for the AO system to compensate for and the throughput for an uncompensated system moves closer to that of a compensated one. The second effect that decreases the relative performance of throughput for a compensated system is the spiking f_G. As the Greenwood frequency approaches and exceeds the AO bandwidth the system can no longer effectively close the controls loop and compensate for the atmosphere. While the bandwidth of an AO system can be increased, the cost can be prohibitive and cost-minded efforts have chosen lower bandwidths that are more

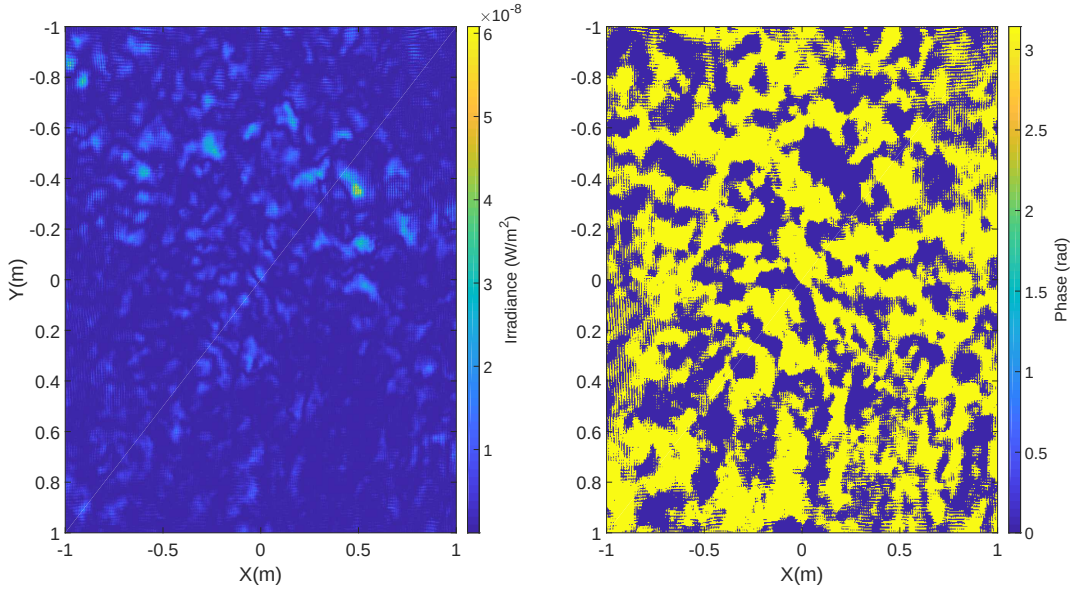

Figure 15. Irradiance (left) and phase (right) of field at front of telescope for $N = 1024$ and $\zeta = 75°$. Significant aliasing effects are seen in both images.

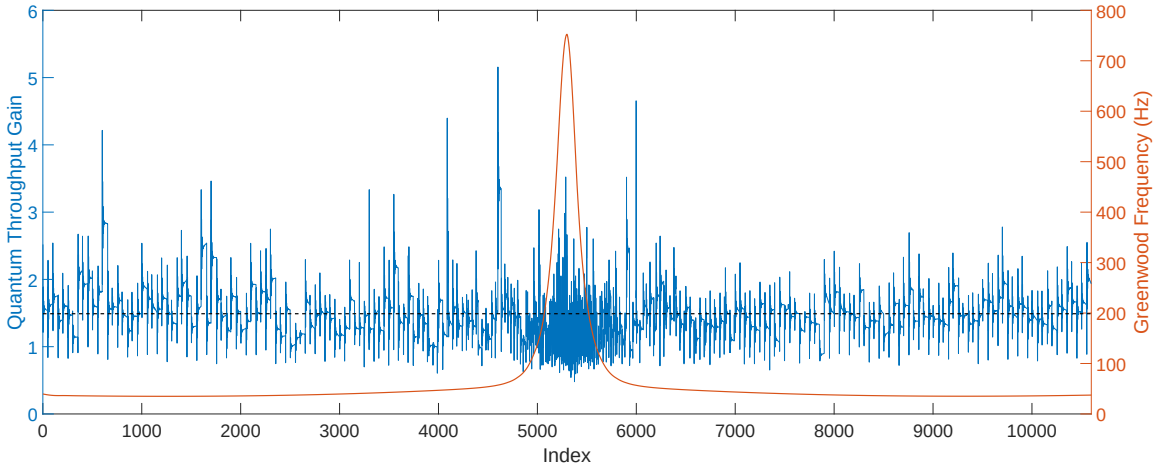

Figure 16. Quantum throughput improvement by using AO. 100 data points taken at 5 second intervals over modeled satellite pass.

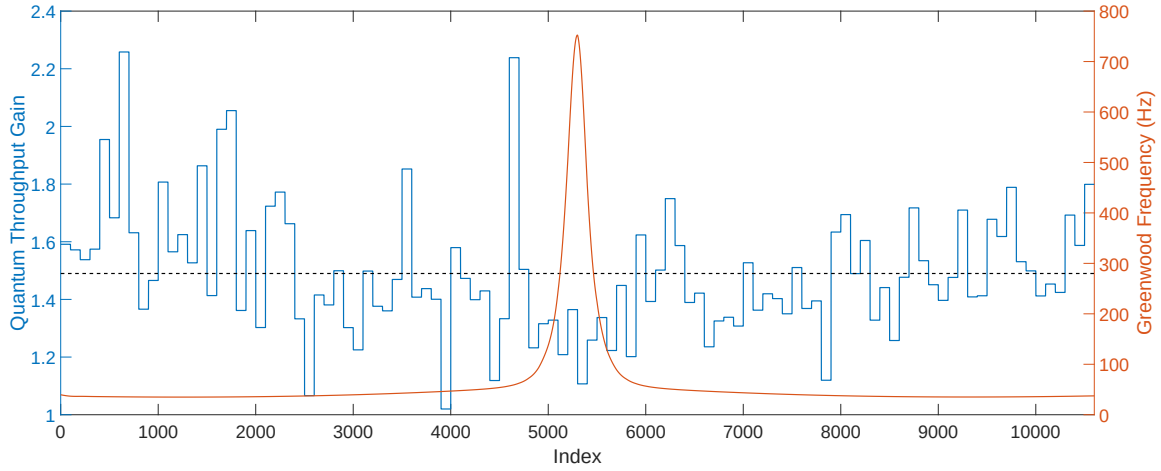

Figure 17. 100 data point average of quantum throughput improvement with AO.

affordable [39].

In order to better average out variations in the simulation, 5,000 data points at three elevation angles are taken. The number of data points chosen was based on the results found in earlier results, where 10,000 data points at a set elevation angle was taken [40]. The variance was reduced when 1,000 data points were averaged and greatly reduced when 5,000 data points were used. Elevation angles of 24.6°, 81.3°, and 84.4° where chosen to allow for large shifts in f_G and r_0. However, the elevation angles of 81.3° and 86.4° share a similar r_0, but the f_G is closer for the 81.3° and 24.6° elevation angles. The f_G, r_0, and σ^2 values for the three elevation angles can be seen in Table 1.

Tables 2, 3, and 4 show the quantum throughput gains when using an AO system at the three different elevation angles. The quantum throughput gains are calculated by dividing the optical throughput with AO by the optical throughput without AO. The number of actu-

Table 1. Atmospheric parameters for elevation angles of 24.6°, 81.3°, and 84.4°.

		r_0(cm)	f_G(Hz)	σ^2
Elevation Angle(°)	24.6	4.55	35	.920
	81.3	8.40	138	.141
	86.4	8.45	752	.139

ators is varied between 16 and 32, and the control loop bandwidth is set at either 500, 1000, or 2000Hz. In Table 2 the largest effect to the quantum throughput is caused by increasing the number of actuators, while changing the bandwidth has little to no effect. This makes sense because all three bandwidths are much greater than the Greenwood frequency. However, with 16 actuators, their effective size is 6.25cm in the primary pupil plane. This is larger than the $r_{0,pw}$ value of 4.55cm. With 32 actuators, their size is 3.13cm, smaller than the $r_{0,pw}$ value. Thus the AO correction effects are significantly better with 32 actuators, no matter the bandwidth.

In Table 3 the number of actuators also seems to have more of an effect than the correction bandwidth. At an elevation angle of 81.3° both numbers of actuators exceed the $r_{0,pw}$ value. Further, all correction bandwidth options are larger than the Greenwood frequency. An improvement of about 33% is seen with increasing the number of actuators while increasing the AO bandwidth results in an improvement of 10% less. However, at an elevation angle of 84.4° the results shift.

In Table 1 the Greenwood frequency spikes to 752Hz at 84.4°. This is much higher than the control bandwidth of 500Hz and almost as high as the bandwidth set to 1 kHz. For this elevation angle increasing the number of actuators only gives an improvement of about 10-30% while increasing the AO bandwidth from 500Hz to 1 kHz gives around a 100% improvement, and the improvement from 500Hz to 2 kHz is about 100-135%. At very high elevation angles increased bandwidth provides more of an improvement relative to increasing the number of actuators.

Table 2. Simulated quantum throughput gain at an elevation angle of 24.6° with varied AO parameters.

		AO Update Rate (Hz)		
		500	1000	2000
Number of Actuators	16	4.20	4.55	4.20
	32	8.58	7.73	7.99

Table 3. Simulated quantum throughput gain at an elevation angle of 81.3° with varied AO parameters.

		AO Update Rate (Hz)		
		500	1000	2000
Number of Actuators	16	3.00	3.00	3.29
	32	4.05	3.99	4.03

Table 4. Simulated quantum throughput gain at an elevation angle of 86.4° with varied AO parameters.

		AO Update Rate (Hz)		
		500	1000	2000
Number of Actuators	16	1.20	2.28	2.43
	32	1.42	2.96	3.35

Thus, the system designer should consider which parameter is more important to the overall quantum throughput. Many satellite passes over a ground site do not get above 86.4°, and those that do spend only seconds above it, while they spend minutes below it. This means in this engagement scenario, where there is significant signal to run the AO system, the number of actuators provides improved throughput gains over AO bandwidth. It is important to note that in a light-starved environment, such as Space Surveillance Operations (SSO), the SNR becomes an important player in an AO system's effectiveness, but that is outside the scope of this set of simulations.

VIII. Experimental Comparison

For this study the model will be compared to a recently published QKD experiment, SOCRATES, performed by a research group based out of Japan [22]. Further studies could also use this model to compare against the recent Chinese experimental results [14–16]. In the experiment two beams were propagated from the Small Optical TrAnsponder (SOTA) terminal on SOCRATES to the ground. The beams had a wavelength of 800nm, a transmit diameter of 5mm and were focused to produce a spot size of 600m at an elevation angle of 53° [22]. The propagated beam was measured with a 1m telescope with a 3mm beam stop, and the space coupling loss was found to be between -56.9 and -57.8dB depending on the beam [22]. With these set parameters, the propagation model is modified to fit the SOCRATES experimental setup.

The first change to the model is in the initial beam and transmit aperture. Instead of having to model the propagation from a fiber through the transmit telescope, the beam can be directly defined at the output of the transmit aperture by making a Gaussian approximation [26]. The intensity distribution and focus of the transmitted beam at the source and after propagation are described by Eqs. (24) and (25) respectively [26]. In Eqs. (24) and (25) r is the distance from the center of the beam, k is the wavenumber, and α_0 is a complex parameter computed in Eq. (26). In Eq. (26) W_0 is half the transmit bean diameter and F_0 is the phase front radius of curvature [26]. F_0 can be computed as shown in Eq. (27), where W is half the final beam diameter. Evaluating Eq. (27) with the SOCRATES parameters gives $F_0 = -6.6917$. Using Eq. (25), when vacuum propagated to the telescope, the loss is found to be -52.85dB, which is close to the experimental value of -57.8dB. The H-$V_{5/7}$ turbulence model is used to add turbulent effects to the beam as it is in Ch. VII. Even though Japan's atmosphere is likely not the same as Colorado's, the H-$V_{5/7}$ is a strong turbulence model that causes scintillation effects to the beam. These scintillation effects were partially blamed for increased beam losses in the experiment [22]. While the Submarine

Laser Communication (SLC) model, based out of data taken in Hawaii, is more likely to model the atmosphere over Japan, it is a weaker turbulence model and would not affect the beam as much as the H-$V_{5/7}$ model [26].

$$U_0(r,0) = e^{-\frac{1}{2}\alpha_0 k r^2} \tag{24}$$

$$U_0(r,z) = \frac{1}{1+j\alpha_0 z} e^{jkz+\frac{jk}{2z}\left(\frac{j\alpha_0 z}{1+j\alpha_0 z}\right)r^2} \tag{25}$$

$$\alpha_0 = \frac{2}{kW_0^2} + j\frac{1}{F_0} \tag{26}$$

$$F_0 = \frac{z}{1-\sqrt{\left(\frac{W}{W_0}\right)^2 - \left(\frac{2z}{kW_0}\right)^2}} \tag{27}$$

Like in Ch. VI a modeled satellite pass was used. However, instead of the Iridium satellite over Boulder, CO, SOCRATES over the National Institute of Information and Communications Technology (NICT) in Tokyo, Japan was modeled. This was done because NICT was the ground station in the experiment [22]. And while the specific pass used in the paper was not modeled, one with a very similar culmination angle was. This gives a very good comparison between the model and experiment.

With turbulent effects added to the beam, the beam loss in the focal plane of the telescope with a 3mm beam stop is found to be -52.84dB, with little difference when compared to the vacuum propagation. This lack of additional loss is due to the beam stop being so large. The PSF at the beam stop can be found by convolving the PSF of the telescope with that of the atmosphere as shown earlier in Ch. V [27, 30]. The OTF of the atmosphere for a given $r_{0,pw}$ and telescope diameter is shown in Eq. (28) and is a variation of Eq. (22) that allows the short-term PSF to be found [27]. In Eq. (28) f_0 is the diffraction limited cutoff frequency, and the value α is set to 0 for the long-term PSF, 1 for the short-term or tilt-removed PSF, or .5 for the short-term PSF with a scintillated beam [27]. The $r_{0,pw}$ value for the path simulated is 7.62cm. The PSF of the telescope system convolved with

the atmosphere's PSF, given the $r_{0,pw}$ value, gives a final long-term PSF of about 100μm. That is much smaller than the field stop used in the experiment [22].

$$H(f) = e^{-3.44\left(\frac{f_{x,y}D}{2f_0 r_0}\right)^{5/3}\left[1-\alpha\left(\frac{f_{x,y}}{2f_0}\right)^{1/3}\right]} \tag{28}$$

Fig. 18 shows a comparison of the short and long-term PSFs. For a beam stop of around 60μm or less tracking provides improved throughput. The improvement is diminished as the field stop radius is increased, and after it reaches a size of 100μm fine tracking provides no advantage. When the field stop is reduced to 100μm in the model the quantum throughput is found to be -53.65dB, very close to the value with the much larger field stop. When the field stop is decreased to 60μm the throughput is decreased to -55.61dB, close to the throughput with the much larger field stop and within the loss range seen in the experiment [22]. Many of the unexpected losses seen in the experiment were likely due to pointing errors of the satellite or polarization misalignment, and not to atmospheric effects.

With the propagation, atmospheric, and satellite components of the model modified to match the experiment, the final part is to compare the tracking and wavefront sensing systems used. Since an AO system was not used in the experiment the SRI system modeled in Ch. V is not used. However, the tracking system is as one was used in the experiment [22]. While light with a different wavelength is used for tracking in the experiment, it would produce the same results as in the model where the same wavelength is used for tracking and in the quantum channel.

A 61 second interval over the center of the satellite pass centered over the culmination angle was used to replicate the experimental data. While this does not simulate the entire link in the experiment, it does match Fig. 5 in [22]. Fig. 19 shows the satellite parameters for the SOCRATES pass used in the simulation. Because the satellite culminates at a much lower elevation angle than the Iridium 5 satellite pass used in Ch. VI, the azimuth and elevation slew rates are considerably more subdued. These effects can be seen in Fig. 20,

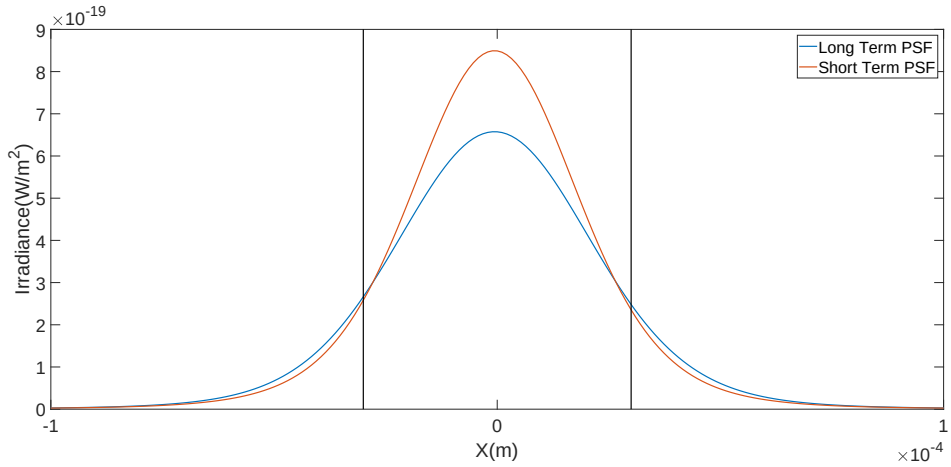

Figure 18. Short and long-term PSF given SOCRATES parameters. Within a radius of about 30μm tracking provides an improvement over a system without fine pointing and tracking.

where the Greenwood frequency does not spike nearly as high at culmination. Since the elevation angle never goes below 54°, the $r_{0,pw}$ stays relatively constant and the scintillation index never goes above .2. While this means some scintillation is present, it is not nearly as severe as it was in the Iridium 5 scenario of Ch. VI.

In the SOCRATES experiment Eq. (29) was used to determine the QBER [22], where $N(y|x)$ refers to the number of counts at detector y given input polarization state x. In order to determine the QBER from the M&S Eq. (30) is used [3]. Because the $N(1|0)$ and $N(0|1)$ results were taken over one second their sum is equal to R_{error} in Eq. (30). R_{sift} is calculated as shown in Eq. (31) where f_{rep} is the source rate, μ is the mean photon number, η is the detection efficiency, and t_{link} is the optical throughout over the entire link [3]. If the only variable assumed to be changing is the atmospheric coupling throughput, then the values can be combined into a constant, C, multiplied by the coupling throughput, $t_{coupling}$. Eq. (32) is used to determine C, where $<>$ denotes expected values. All 12 seconds of data are used to determine the mean QBER of .0424 and an R_{error} of 214.232bits/sec. The mean of the quantum throughput in the 12 second interval around culmination is used to estimate $t_{coupling}$. The $t_{coupling}$ value is estimated to be $6.5979 * 10^{-6}$ giving a C value of $7.333 * 10^{8}$.

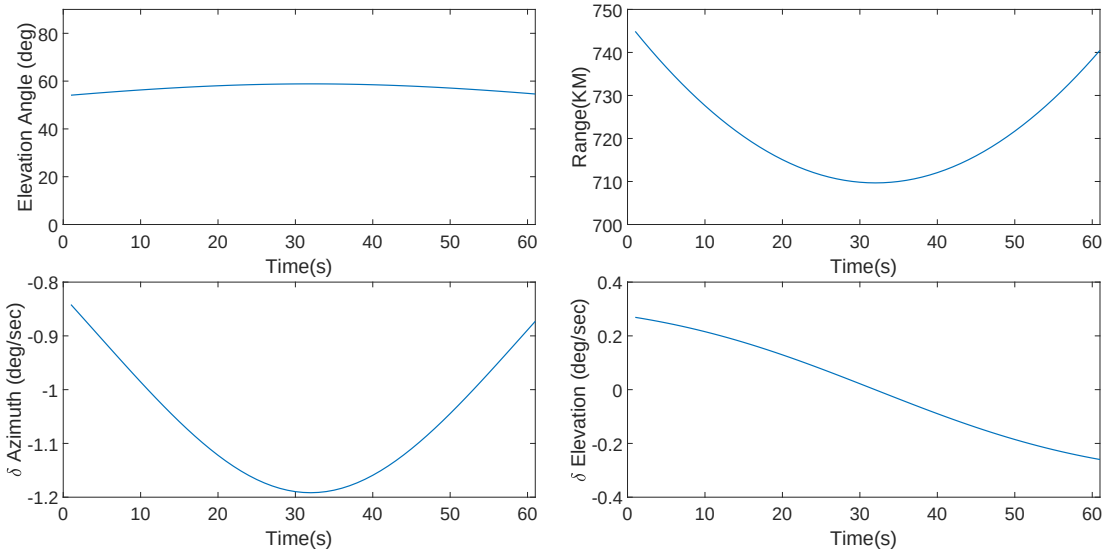

Figure 19. Satellite parameters of SOCRATES pass over NICT in Japan. Data collected at 1s intervals.

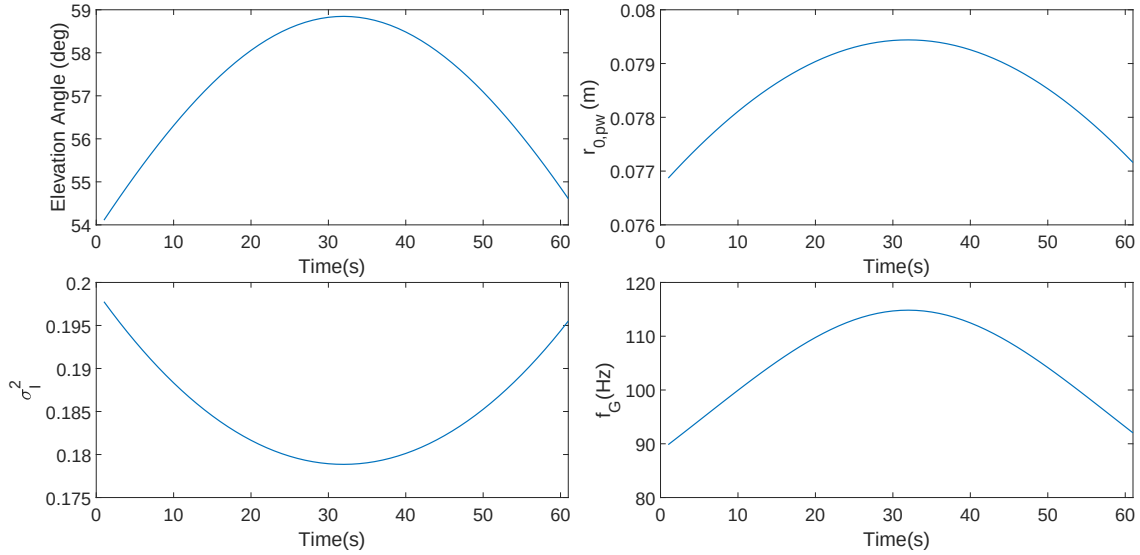

Figure 20. Atmospheric parameters of SOCRATES pass over NICT in Japan.

$$QBER = \frac{N(1|0)+N(0|1)}{\sum_{x=0,1}\sum_{y=0,1}N(y|x)} \tag{29}$$

$$QBER = \frac{R_{error}}{R_{sift}+R_{error}} \tag{30}$$

$$R_{sift} = \frac{1}{2} f_{rep} \mu t_{link} \eta \approx C * t_{coupling} \tag{31}$$

$$< QBER >= \frac{< N(1|0)+N(0|1) >}{< N(1|0)+N(0|1) > + C * < t_{coupling} >} \tag{32}$$

Fig. 21 shows the QBER over the satellite pass. Each QBER data point is the mean of 2000 data points taken at each 1s interval of the satellite pass. A larger number of data points were not used due to time constraints on the simulation. The QBER with a 3mm beam stop falls within the range of experimental values where the polarization compensation method worked [22]. However, because polarization compensation failed outside of the 12s interval in the experiment, the model showed a much lower QBER outside of the 12s range. If the polarization had been adequately compensated for through the entire pass it is expected that the experimental and simulated results would better match throughout the pass. Fine pointing and tracking did not affect the QBER with either the 3mm or 60μm beam stops. This was expected with the 3mm beam stop, beacuse the beam stop is much larger that the expected PSF. From Fig. 18 no throughput improvement is expected from the addition of fine pointing until reducing the beam stop below 100μm. But the result is slightly surprising for the 60μm beam stop. It is likely that the beam stop needed to be narrower than 60μm for tracking to show an improvement. However, with a 60μm beam stop, the QBER was already at the upper limit for a QKD protocol to be able to generate a key [3]. This means that while higher-order AO allows for a reduction in the beam stop while keeping the quantum throughput within the necessary bounds, tracking on its own does not. However there are still benefits to having a fine pointing and tracking system.

Fig. 22 shows the variance of the QBER at each point over the satellite pass. The

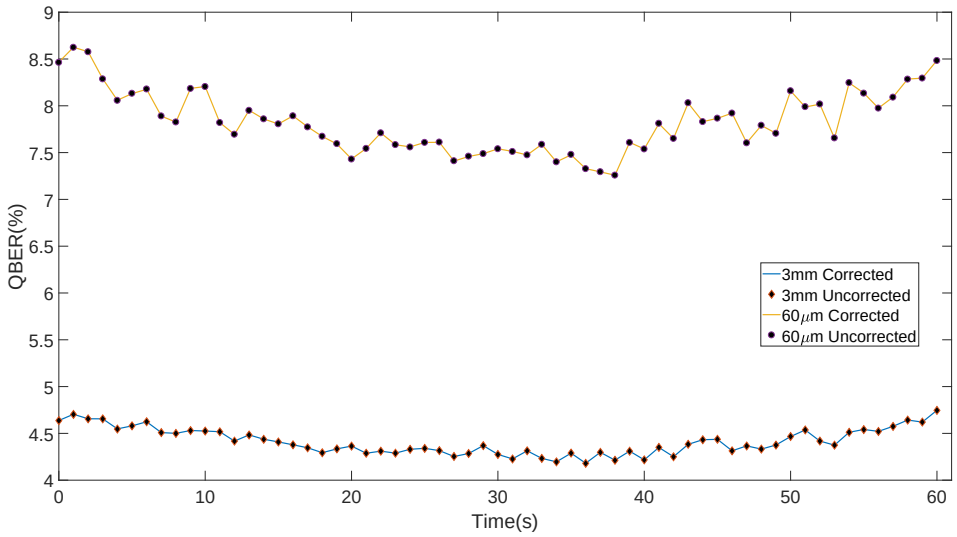

Figure 21. QBER of modeled for different beam stop diameters with and without fine pointing and tracking. QBER is average of 2000 data points taken at each 1s interval of the satellite pass.

variance with the 60μm beam stop has a lot of variance because part of the beam is blocked. And while the beam is not heavily scintillated, there is enough scintillation to vary the amount of irradiance that passes through the beam stop. The variance with the 3mm beam stop is almost constant by comparison. This is because very little energy is lost outside the beam stop. However there are sources of error that would increase the variance for the case without pointing and tracking. The telescope is modeled as pointing at the satellite without any course pointing and tracking error. And no effects of wind buffeting the telescope are modeled either. Further, pointing errors caused by buildings being pushed by the wind or general vibrations within a building would also be compensated for by fine pointing and tracking systems [41]. So, while fine pointing and tracking does not necessarily allow for a reduction in the beam stop from atmospheric effects, it still plays an important part in an overall system free-space QKD system.

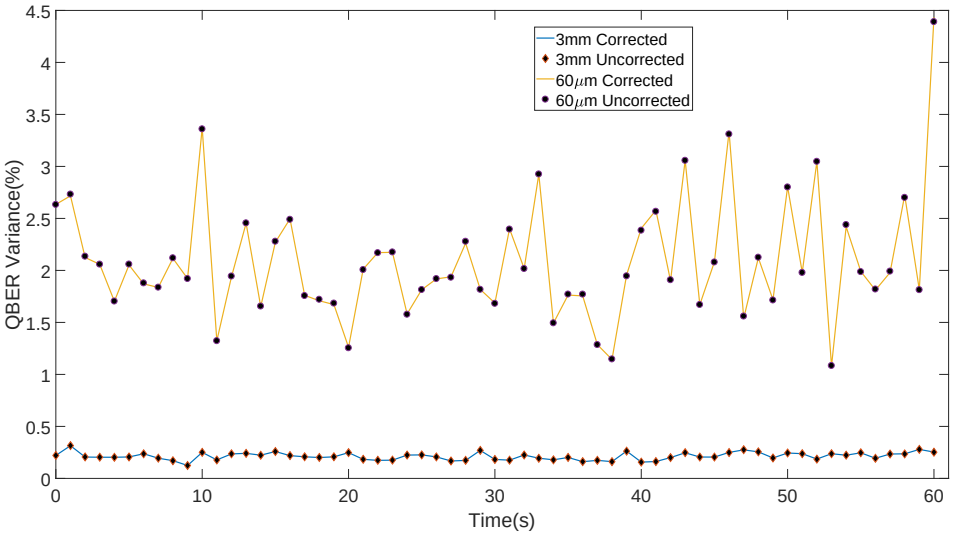

Figure 22. Variance of QBER with different beam stop diameters and with or without fine pointing and tracking. Variance is over 2000 data points taken at each 1s interval of the satellite pass.

IX. Conclusion

Quantum algorithms provide a potentially important area of impact for science and security over the next several decades. Not only do QKD protocols provide a means for secure key generation between two separated locations, but entanglement algorithms allow for a better understanding of quantum physics [3, 42–44]. But in order for these protocols to fully affect the current status quo, they must be made more resilient. While multiple free-space experiments have been completed, and many more will be performed, M&S efforts can provide necessary support alongside the experimental efforts. [1–16, 22, 39, 41]. Moreover, these models need to model both the key generation and atmospheric effects as discrete effects; if this is not done, the modeling results will tend to vary dramatically from experimental results where finite key lengths result in a wide variance of results.

In this thesis a free-space propagation model was built to study the impact of AO on QKD free-space experiments. The model not only includes atmospheric effects, but the effects of satellite passes as well as the correction effects of fine pointing and tracking systems as well as higher-order AO systems. The results from the model are compared to analytic expectations in order to understand the validity of the model. Then a series of simulations are run with varying AO system parameters to better understand the robustness of the model as well as provide insight into the AO system specification trade space and its effect on the quantum throughput. The high amount of variance seen in the quantum throughput underscores the necessity of simulating the atmosphere as a set of discrete events and not treating it just by its long term average effects. Finally, the model was compared to a recent satellite experiment [22].

9.1 Future Work

While the propagation model compared well to the free-space losses encountered in the experiment, variances in the quantum algorithm, specifically polarization compensation, caused the experimental and modeling results to diverge. This divergence should be studied in future work. Specific recommendations include; modeling the satellite's reference frame relative to the ground station; studying polarization measurement and compensation performed in the telescope, and performing an end-to-end simulation of the QKD protocol to explore the effects of polarization compensation effectiveness on quantum throughput. Finally, phase unwrapping and guard bands should be introduced into the AO system model to better represent an operational AO system.

Bibliography

1. J-P. Bourgoin, E. Meyer-Scott, B. L. Higgins, B. Helou, C. Erven, H. Hbel, B. Kumar, D. Hudson, I. DSouza, R. Girard, R. Laflamme, and T. Jennewein, "Corrigendum: A comprehensive design and performance analysis of low earth orbit satellite quantum communication," New Journal Of Physics, vol. 16, pp. 145–195, 2014.

2. T. Schmitt-Manderbach, H. Weier, M. Furst, R. Ursin, F. Tiefenbacher, T. Scheidl, T. Perdigues, Z.s Sodnik, C. Kurtsiefer, J. G. Rarity, A. Zeilinger, and H. Weinfurter, "Experimental demonstration of free-space decoy-state quantum key distribution over 144km," Physics Review Letters, vol. 98, 2007.

3. N. Gisin, G. Ribordy, W. Tittel, and H. Zbinden, "Quantum cryptography," Review Of Modern Physics, vol. 74, pp. 145–195, 2002.

4. L. O. Mailloux, R. D. Engle, M. R. Grimaila, D. D. Hodson, J. M. Colomi, and C. V. McLaughlin, "Modeling decoy state quantum key distribution systems," Journal of Defense Modeling and Simulation: Application, Methodology, Technology, vol. 12, pp. 489–506, 2015.

5. C. Peng, T. Yang, X. Bao, J. Zhang, X. Jin, F. Feng, B. Yang, J. Yang, J. Yin, Q. zhang, N. Li, B. Tian, and J. Pan, "Experimental free-space distribution of entangled photon pairs over 13km: Towards satellite-based global quantum communication," Physics Review Letters, vol. 94, 2005.

6. G. Vallone, D. Bacco, D. Dequal, S. Gaiarin, V. Luceri, G. Bianco, and P. Villoresi, "Experimental satellite quantum communications," Physics Review Letters, vol. 115, 2015.

7. CJ. Wang, B. Yang, S. Liao, L. Zhang, Q. Shen, X. Hu, J. Wu, S. Yang, H. Jiang, Y. Tang, B. Zhong, H. Liang, W. Liu, Y. Hu, Y. Huang, B. Qi, J. Ren, G. Pan, J. Yin, J. Jia, Y. Chen, K. Chen, C. Peng, and J. Pan, "Direct and full-scale experimental verifications towards ground-satellite quantum key distribution," Nature Photonics, vol. 7, 2013.

8. A. Carrasco-Casado, H. Kunimori, H. Takenaka, T. Kubo-Oka, M. Akioka, T. Fuse, Y. Koyama, D. Kolev, Y. Munemasa, and M. Toyoshima, "Leo-to-groiund polarization measurements aiming for space qkd using small optical transponder (sota)," Optics Express, vol. 24, 2016.

9. S. Liao, H. Yong, C. Liu, G. Shentu, D. Li, H. Dai, S. Zhao, B. Li, J. Guan, W. Chen, Y. Gong, Y. Li, Z. Lin, G. Pan, J. S. Pelc, M. M. Fejer, W. Zhang, W. Liu, J. Yin, J. Ren, X. Wang, Q. Zhang, C. Peng, and J. Pan, "Ground test of satellite constellation based quantum communication," 2016, preprint, `http://arxiv.org/abs/1611.09982`.

10. M. T. Gruneisen, B. A. Sickmiller, M. A. Flanagan, J. P. Black, K. E. Stoltenberg, and A. W. Duchane, "Adaptive spatial filtering of daytime sky noise in a satellite quantum key distribution downlink receiver," Optical Engineering, vol. 55, 2014.

11. M. T. Gruneisen, B. A. Sickmiller, M. A. Flanagan, J. P. Black, K. E. Stoltenberg, and A. W. Duchane, "Modeling daytime sky access for a satellite quantum key distribution downlink mark," Optical Society of America, vol. 23, 2015.

12. R. J. Hughes, J. E. Nordholt, D. Derkacs, and C. G. Peterson, "Practical free-space quantum key distribution over 10 km in daylight and at night," New Journal of Physics, vol. 4, 2002.

13. X. Sun, I. B. Djordjevic, and M. A. Neifeld, "Secret key rates and optimization of bb84 and decoy state protocols over time-varying free-space optical channels," IEEE Photonics, vol. 8, 2016.

14. Juan Yin, Yuan Cao, Yu-Huai Li, Sheng-Kai Liao, Liang Zhang, Ji-Gang Ren, Wen-Qi Cai, Wei-Yue Liu, Bo Li, Hui Dai, Guang-Bing Li, Qi-Ming Lu, Yun-Hong Gong, Yu Xu, Shuang-Lin Li, Feng-Zhi Li, Ya-Yun Yin, Zi-Qing Jiang, Ming Li, Jian-Jun Jia, Ge Ren, Dong He, Yi-Lin Zhou, Xiao-Xiang Zhang, Na Wang, Xiang Chang, Zhen-Cai Zhu, Nai-Le Liu, Yu-Ao Chen, Chao-Yang Lu, Rong Shu, Cheng-Zhi Peng, Jian-Yu Wang, and Jian-Wei Pan, "Satellite-based entanglement distribution over 1200 kilometers," Science, vol. 356, no. 6343, pp. 1140–1144, 2017.

15. S. Liao, W. Cai, W. Liu, L. Zhang, Y. Li, J. Ren, J. Yin, Q. Shen, Y. Cao, Z. Li, F. Li, X. Chen, L. Sun, J. Jia, J. Wu, X. Jiang, J. Wang, Y. Huang, Q. Wang, Y. Zhou, L. Deng, T. Xi, L. Ma, T. Hu, Q. Zhang, Y. Chen, N. Liu, X. Wang, Z. Zhu, C. Lu, R. Shu, C. Peng, J. Wang, and J. Pan, "Satellite-to-ground quantum key distribution," 2017, preprint, https://arxiv.org/abs/1707.00542v1.

16. J. Ren, P. Xu, H. Yong, L. Zhang, S. Liao, J. Yin, W. Liu, W. Cai, M. Yang, L. Li, K. Yang, X. Han, Y. Yao, J. Li, H. Wu, S. Wan, L. Liu, D. Liu, Y. Kuang, Z. He, P. Shang, C. Guo, R. Zheng, K. Tian, Z. Zhu, N. Liu, C. Lu, R. Shu, Y. Chen, C. Peng, J. Wang, and J. Pan, "Ground-to-satellite quantum teleportation," 2017, preprint, https://arxiv.org/abs/1707.00934.

17. J. Bourgoin, N. Gigov, B. Higgins, Zhizhong Z. Yan, E. Meyer-Scott, A. Khandani, N. Lütkenhaus, and T. Jennewein, "Experimental quantum key distribution with simulated ground-to-satellite photon losses and processing limitations," Phys. Rev. A, vol. 92, pp. 052339, Nov 2015.

18. V. Scarani and C. Kurtsiefer, "The black paper of quantum cryptography: Real implementation problems," Theoretical Computer Science, vol. 560, pp. 27 – 32, 2014, Theoretical Aspects of Quantum Cryptography celebrating 30 years of BB84.

19. V. Scarani, H. Bechmann-Pasquinucci, N. J. Cerf, M. Dusek, N. Lutkenhaus, and M. Peev, "The security of practical quantum key distribution valerio," Cornell University Library, 2009, https://arxiv.org/abs/0802.4155v3.

20. J. Johnson, "An analysis of error reconciliation protocols for use in quantum key distribution," M.S. thesis, Air Force Institute of Technology, 2012.

21. R. E. Hufnagel, "Propagation Through Atmospheric Turbulence," in The Infrared Handbook, G. J. Zissis and W. L. Wolfe, Eds., chapter 6. INFRARED INFORMATION AND ANALYSIS CENTER ANN ARBOR MI, Washington, DC, 1974, http://www.dtic.mil/docs/citations/ADA100015.

22. H. Takenaka, A. Carrasco-Casado, M. Kitamura, M. Sasaki, and M. Toyoshima, "Satellite-to-ground quantum-limited communication using a 50-kg-class microsatellite," Nature Photonics, vol. 11, 2017.

23. G. Vallone, D. Dequal, M. Tomasin, F. Vedovato, M. Schiavon, V. Luceri, G. Bianco, and P. Villoresi, "Interference at the single photon level along satellite-ground channels," Physical Review Letters, vol. 116, 2016.

24. R. Q. Fugate, J. M. Spinhirne, J. F. Moroney, R. A. Cleis, M. D. Oliker, B. R. Boeke, B. L. Ellerbroek, C. H. Higgins, R. E. Ruane, D. W. Swindle, M. P. Jelonek, W. J. Lange, A. C. Slavin, W. J. Wild, D. M. Winker, and J. M. Wynia, "Two generations of laser-guide-star adaptive-optics experiments at the starfire optical range," J. Opt. Soc. Am. A, vol. 11, no. 1, pp. 310–324, Jan 1994.

25. R. Fugate, Adaptive Optics, vol. 3, Tuscon, AZ, 2001.

26. L. C. Andrews and R. L. Phillips, Laser Beam Propagation through Random Media, SPIE, Bellingham, WA, 2005, ISBNs: 0-8194-5948-8 (Electronic).

27. J. D. Schmidt, Numerical Simulation of Optical Wave Propagation With examples in MATLAB, SPIE, Bellingham, Wa, 2010, ISBNs: 978-0-8194-8326-3 (Electronic).

28. J. L. Bufton, P. O. Minott, M. W. Fitzmaurice, and P. J. Titterton, "Measurements of turbulence profiles in the troposphere," J. Opt. Soc. Am., vol. 62, no. 9, pp. 1068–1070, Sep 1972.

29. J. W. Goodman, Introduction To Fourier Optics, Roberts and Company, Englewood, CO, 2005.

30. R. D. Richmond and S. C. Cain, Direct-Detection LADAR Systems, SPIE, Bellingham, Wa, 2010, ISBNs: 978-0-8194-8072-9 (alk. Paper).

31. P. Anbalagan, M. Sundarambal, and A. V. Hari Prasad Reddy, Development of Interpolation Algorithms for Multirate Signal/Image Processing, New Delhi, 1998.

32. R. K. Tyson and B. W. Frazier, Field Guide to Adaptive Optics, SPIE, Bellingham, WA, Second edition, 2012, ISBNs: 978-0-8194-9017-9 (Electronic).

33. Spiricon Inc., "Hartmann wavefront analyzer tutorial," Online, 2004.

34. I. J. Thorton, "Development of adaptive tilt tracker that utilizes quadrant-cell detector to track extended objects," M.S. thesis, Air Force Institute of Technology, 2014.

35. T. R. Ellis and J. D. Schmidt, "Wavefront sensor performance in strong turbulence with an extended beacon," in 2010 IEEE Aerospace Conference, March 2010, pp. 1–10.

36. Troy R. Ellis and Jason D. Schmidt, "Hybrid wavefront sensor for strong turbulence," in Frontiers in Optics 2008/Laser Science XXIV/Plasmonics and Metamaterials/Optical Fabrication and Testing. 2008, p. FMF2, Optical Society of America.

37. D. A. Vallado, Fundamentals of Astrodynamics and Applications, Microcosm Press, Hawthorne, CA, 2013, ISBNs: 978-1881883179(hb).

38. "Iridium," `https://www.iridium.com/`, Accessed: 2017-11-20.

39. M. T. Gruneisen, M. A. Flanagan, and B. A. Sickmiller, "Modeling satellite-earth quantum channel downlinks with adaptive- optics coupling to single-mode fibers," Optical Engineering, vol. 56, 2018.

40. Alexander W. Duchane, Douglas D. Hodson, and Logan O. Mailloux, "Modeling a space-based quantum link that includes an adaptive optics system," 2017.

41. V. Fernandez, J. Gmez-Garca, A. Ocampos-Guilln, and A. Carrasco-Casado, "Correction of wavefront tilt caused by atmospheric turbulence using quadrant detectors for enabling fast free-space quantum communications in daylight," IEEE Access, vol. PP, no. 99, pp. 1–1, 2018.

42. A. Einstein, B. Podolsky, and N. Rosen, "Can quantum-mechanical description of physical reality be considered complete," Physical Review, vol. 47, pp. 777–780, 1935.

43. J. S. Bell, "On the Einstein Podolsky Rosen paradox," Physics, vol. 1, pp. 195–200, 1964.

44. J. F. Clauser, M. A. Horne, A. Shimony, and R. A. Holt, "Proposed experiment to test local hidden-variable theories," Physical Review Letters, vol. 23, pp. 880–884, 1969.

REPORT DOCUMENTATION PAGE

Form Approved
OMB No. 0704–0188

1. REPORT DATE *(DD–MM–YYYY)*	2. REPORT TYPE	3. DATES COVERED *(From — To)*
03–22–2018	Master's Thesis	Sept 2017 — Mar 2018

4. TITLE AND SUBTITLE

Modeling a Space-Based Quantum Link

5a. CONTRACT NUMBER

5b. GRANT NUMBER

5c. PROGRAM ELEMENT NUMBER

6. AUTHOR(S)

Duchane, Alexander, W, Capt, USAF

5d. PROJECT NUMBER

5e. TASK NUMBER

5f. WORK UNIT NUMBER

7. PERFORMING ORGANIZATION NAME(S) AND ADDRESS(ES)

Air Force Institute of Technology
Graduate School of Engineering and Management (AFIT/EN)
2950 Hobson Way
WPAFB OH 45433-7765

8. PERFORMING ORGANIZATION REPORT NUMBER

AFIT-ENG-MS-18-M-020

9. SPONSORING / MONITORING AGENCY NAME(S) AND ADDRESS(ES)

Intentionally left blank

10. SPONSOR/MONITOR'S ACRONYM(S)

11. SPONSOR/MONITOR'S REPORT NUMBER(S)

12. DISTRIBUTION / AVAILABILITY STATEMENT

DISTRIBUTION STATEMENT A:
APPROVED FOR PUBLIC RELEASE; DISTRIBUTION UNLIMITED.

13. SUPPLEMENTARY NOTES

14. ABSTRACT

This research first reviews previous and current efforts in free-space Quantum Key Distribution. Next, the propagation and atmospheric simulation techniques used to model the propagation of an optical pulse from a LEO satellite to ground through turbulence are described. An Adaptive Optics system, including both lower order tracking as well as higher order corrections using a Self-Referencing Interferometer, is modeled to correct for the aberrations caused by the atmosphere. The propagation, atmospheric, and Adaptive Optics models are then combined to produce an optical propagation toolkit. The Simplified General Perturbations toolkit is then used to model an Iridium satellite passing over Boulder, CO. Finally, the results from the Simplified General Perturbations toolkit are integrated with the optical propagation toolkit to show the effects of using an Adaptive Optics system over a realistic satellite pass.

15. SUBJECT TERMS

Quantum Key Distribution, Atmospheric Propagation, Phase Screens, Fresnel Propagation, Statistical Optics, Angular Spectrum Propagation, Rayleigh-Summerfeld, Coherence Factor, Structure Function

16. SECURITY CLASSIFICATION OF:			17. LIMITATION OF ABSTRACT	18. NUMBER OF PAGES	19a. NAME OF RESPONSIBLE PERSON
a. REPORT	b. ABSTRACT	c. THIS PAGE			Dr. Douglas D. Hodson, AFIT/ENG
U	U	U	UU	63	19b. TELEPHONE NUMBER *(include area code)* (937) 785-3636 x4719; Douglas.Hodson@afit.edu